Quantitative Analysis of Anisotropic Edge Retraction During Solid-State Dewetting of Thin Single Crystal Films

by

Gye Hyun Kim

B.S., Materials Science and Engineering

University of California at Berkeley, 2010

Submitted to the Department of Materials Science and Engineering

in partial fulfillment of the requirements for the degree of

Master of Science in Materials Science and Engineering

at the

MASSACHUSETTS INSTITUTE OF TECHNOLOGY

September 2012

Signature of Author .....

Department of Materials Science and Engineering
August 22, 2012

Certified by .....

Carl V. Thompson

Stavros Salapatas Professor of Materials Science and Engineering
Thesis Advisor

Accepted by .....

Gerbrand Ceder

R.P. Simmons Professor of Materials Science and Engineering
Chair, Departmental Committee on Graduate Students

Quantitative Analysis of Anisotropic Edge Retraction

During Solid-State Dewetting of Thin Single Crystal Films

by

Gye Hyun Kim

Submitted to the Department of Materials Science and Engineering

on August 22, 2012 in partial fulfillment of the requirements for the degree of

Master of Science in Materials Science and Engineering

Abstract

In the as-deposited state, thin films are generally far from equilibrium and will agglomerate or dewet to form arrays of islands when sufficient atomic motion is allowed. Dewetting can occur well below the films' melting temperature in the solid-state. The dewetting process begins by formation and motion of film-substrate-vapor three-phase boundaries. These film edges retract via capillarity-driven mass transport. In the absence of film or substrate patterning, the dewetting morphology of polycrystalline films is not well ordered. However, dewetting in single crystal films leads to a much more regular morphology, due to surface and interfacial energy anisotropy and surface self-diffusivity anisotropy. When dewetting of such films is templated by pre-patterning, dewetting patterns much smaller than the original template patterns can be generated. This makes templated dewetting a potential self-assembly method for generation of complex structures with sub-lithographic length scales. However, control of such patterns in single crystal films requires a significant degree of quantitative understanding of anisotropic dewetting in the solid-state.

As a starting point for quantitative research on solid-state dewetting of single crystal films, dewetting of thin single crystal films that were pre-patterned to have edges with specific in-plane orientations were quantitatively characterized and their observed behavior was modeled. Edges aligned to specific crystallographic orientations remain straight as they retract, while edges with other crystallographic orientations develop in-plane facets composed of kinetically stable edges. Therefore, a quantitative understanding of the retraction of kinetically stable edges can serve as the basis for understanding the retraction of edges with all other orientations. Measurements of the rates of retraction of kinetically stable edges for single crystal (100) and (110) Ni films on single crystal MgO are reported. In cross section, the retracting edges develop out-of-plane facets that are generally consistent with the facets expected from the equilibrium Wulff shape. To capture the observed anisotropic character of the edge retraction rate, capillarity-driven edge retraction through atomic surface self-diffusion was modeled in 2 dimensions using the crystalline formulation method developed by Carter and coworkers. The model and experiments show a similar time scaling for the edge retraction distance. Also, the magnitudes of the predicted retraction rates are consistent with the specific observed retraction rate anisotropy given the large range of error in parameters used in the model. Other possible sources of error include the fact that actual edges are not fully facetted and are sometimes bound by non-equilibrium facets.

Thesis Advisor: Carl V. Thompson

Title: Stavros Salapatas Professor of Materials Science and Engineering

Acknowledgement

My advisor Carl certainly is the one I have to thank first and the most. Without his help and guidance, this work would not have been possible. He has been the best resource during my pursuit of science at MIT and he also will be. I would also like to thank my doctoral thesis committee members, Professor Carter and Professor Ross, and the chair of my thesis area examination committee, Professor Allen, for the fruitful guidance. I also thank my group members, collaborators, and the shared experimental facility staff, especially Rachel, for the help and advice that became the core of this thesis.

Last but not least, my sincere gratitude to my family and Victoria, who have always been supportive from the opposite side of the globe. My life has always been brighter and happier with your presence.

Table of Contents

List of Tables

List of Figures

Figure 2-1. Schematic illustration of HRXRD scan settings. Each parameter was carefully adjusted to maximize signal from the epitaxial film.

Figure 2-2. (a) 2θ-ω scan of Ni(100) film. (b) 2θ-ω scan of Ni(110) film. (c) (111) in-plane peak of MgO(100). (d) (111) in-plane peak of Ni(100) deposited on MgO(100). (e) (111) in-plane peak of MgO(110). (f) (111) in-plane peak of Ni(110) deposited on MgO(110).

Figure 4-1. Illustration of the template pattern to be used in the experiment. The patches were designed to align along kinetically stable retraction orientations, which are defined as the retraction orientations in which no in-plane faceting during edge retraction occurs.

Figure 4-2. Edges in Ni(100) films after retracting during a 3-hour anneal at 900 °C under a reducing gas flow rate of 2330 sccm. In (a), the original edge was straight and was aligned at a 35° rotation away from the in-plane [001] orientation. In this case the edge breaks up into kinetically stable in-plane facets. The edge aligned along the [001] direction in (b) is kinetically stable. The in-plane facets in (a) lie along [001] and [110] orientations, both of which are kinetically stable during retraction. Scale bars are 10 μm long.

Figure 4-3. Schematic diagram of the edge retraction in non-kinetically stable orientations. The dashed lines in the figure indicate the macroscopic orientation of the edge. During retraction, the edge becomes unstable and is decomposed into an alternating row of kinetically stable facets 1 and 2.

Figure 4-4. Retraction rates of kinetically stable edges for Ni(100) and Ni(110) films. The samples were annealed at 900 °C under a 2310 sccm reducing gas (5% H_2 95% N_2) flow. The exponents for power law fits are also given. Appropriate equilibrium Winterbottom shapes were obtained using *The Wulffmaker*, a program for equilibrium shape generation.

Figure 4-5. SEM images of the cross-sections of retracting edges in (a) and (b) Ni (100) films, and (c) and (d) Ni(110) films after 21-hour annealing at 900 °C. Retraction directions and facet planes are indicated. Scanning angle (angle between the electron beam and the cross section) is 52 degrees. Equilibrium facets comprising the Wulff shape of Ni appear, but some nonequilibrium facets also appear during retraction.

Figure 4-6. Power law fit exponents for experimental retraction data. Error bars of the exponents are constructed by calculating a 99% confidence interval using a t-distribution statistics multiplied by the standard error for the exponent.

Figure 4-7. AFM images of growing natural holes in Ni(100) and Ni(110) films under 2310 sccm reducing gas condition. The annealing times are indicated in the images. (a) and (b) Growth of natural holes in Ni(100). (c) and (d) Growth of natural holes in Ni(110).

Figure 5-1. Illustration of convexity factor calculation. Convexity factors in 2-dimensional shapes are determined by the relationship of the facet of interest with its adjacent facets.

Figure 5-2. Equilibrium Winterbottom shapes. (a) Winterbottom shape for patches in Ni(100) retracting in [010]. (b) Winterbottom shape for patches in Ni(100) retracting in [011]. (c) Winterbottom shape for patches in Ni(110) retracting in $[1\bar{1}0]$. (d) Winterbottom shape for

Chapter 1. Introduction

Thin solid films are generally far from equilibrium in the as-deposited state, except for very unusual circumstances, and therefore are unstable or at most metastable. Thus, when such films are heated to a sufficiently high temperature to allow enough atomic mobility, surface diffusion allows the film to lower its energy by agglomerating or dewetting to form arrays of islands. This dewetting phenomenon can occur well below the films' melting temperature and it has historically been an issue in microelectronics industry; consequently, much effort has been invested to prevent it from occurring [1, 2]. On the other hand, recent research shows that dewetting can also be used to make arrays of particles for many applications, including, but not limited to, sensors [3], catalysts for carbon nanotube growth [4], and those for semiconductor nanowires [5].

When a thin film is deposited on a substrate, three different interfaces exist: the film-vapor, the substrate-vapor, and the film-substrate interfaces. Toward equilibrium, the agglomerating film evolves into a morphology that minimizes the total energy of the system, and this is conveniently expressed in terms of the energies of these interfaces in Young's equation [6], assuming isotropic interfacial energies:

$$\gamma_{sv} = \gamma_{fs} + \gamma_{fv} \cos\theta \qquad (1\text{-}1)$$

where γ_{sv} refers to the substrate-vapor interfacial energy, γ_{fs} the film-substrate interfacial energy, and γ_{fv} the film-vapor interfacial energy. For films with isotropic energies, this determines the equilibrium contact angle at the three-phase boundary and thus the equilibrium shape will be a spherical cap, as shown in Figure 1-1. When the equilibrium contact angle θ is zero, the film can cover or wet the entire substrate and remain thermodynamically stable. For all other nonzero contact angles, the film experiences a thermodynamic driving force to dewet.

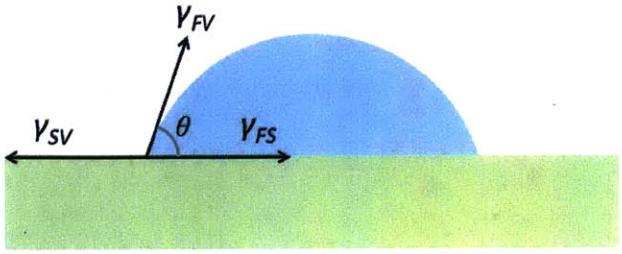

Figure 1-1. Schematic diagram of the equilibrium shape of an island on a substrate with isotropic energies.

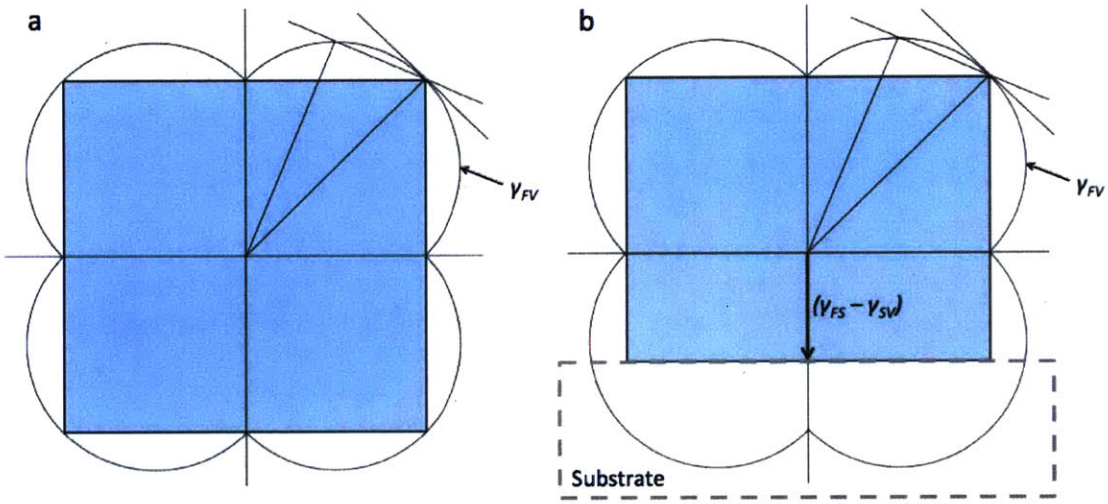

Figure 1-2. **(a)** The Wulff-Herring construction and **(b)** the Winterbottom construction.

For materials with anisotropic surface and interfacial energies, the equilibrium shape can be computed by the Wulff-Herring [7, 8] and the Winterbottom [9] constructions. As illustrated in Figure 1-2(a), the equilibrium Wulff shape of a free-standing material can be found by obtaining the envelope of lines in 2-dimension, and planes in 3-dimension, drawn normal to the line originating from the center of the anisotropic film-vapor interfacial energy curve in all orientations. For thin-film structures, a substrate-film interface needs to be introduced and the energy has to be adjusted at the interface, and this can be done by the Winterbottom construction,

as illustrated in Figure 1-2(b). The film-vapor interfacial energy in the direction normal to the film-substrate interface is replaced by the vector having the same normal but its magnitude is decreased by the adhesion energy of the film-substrate interface.

Because the nature of dewetting is retraction of a film on a substrate to form agglomerates, it is necessary to have some portion of the substrate exposed and have a three-phase contact of the film, the substrate, and the vapor to initiate dewetting. Therefore, dewetting initiates either at pre-existing holes or film edges, or after natural holes are formed. Pre-patterning the film before allowing it to dewet is one way to form three-phase boundaries. Pre-existing holes or defects large enough to expose the substrate-vapor interface are also where dewetting can initiate. Even in films without any pre-existing holes or patterned edges, however, dewetting usually occurs at elevated temperatures. In this case, dewetting is followed by the formation of natural holes that expose the substrate-vapor interface and form the three-phase boundary. For an infinite defect-free planar surface with isotropic surface energies without any stress effects, Mullins [10] showed that the surface is stable against all perturbations where a linear stability analysis is applicable. This also holds in the case of the surface of a film on a substrate whose equilibrium shape is an island, if the amplitude of the perturbation is smaller than the film thickness. Generally, however, thin films are not perfectly defect-free, and it is accepted that defects in the films allow easier natural hole formation. For instance, Srolovitz and Safran [11] studied the growth of grooves at idealized 2-dimensional grain boundaries by capillarity-induced surface self-diffusion, as schematically illustrated in Figure 1-3.

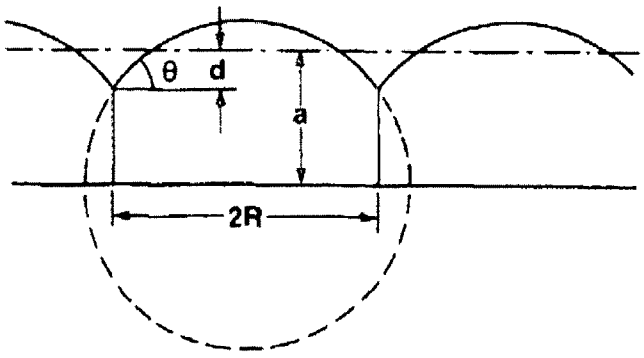

Figure 1-3. Growth of grooves at grain boundaries by capillarity-induced surface self-diffusion, after Srolovitz and Safran [11].

Using a similar construction as in Figure 1-1, it is found that the groove angle θ, in thermodynamic equilibrium, is:

$$\theta = sin^{-1}(\frac{\gamma_{gb}}{2\gamma_{fv}}), \tag{1-2}$$

where γ_{gb} refers to the grain boundary energy and γ_{fv} the film-vapor interfacial energy. When equilibrium is reached, grooves of depth d will form, which can be geometrically calculated [11]:

$$d = R\frac{2-\cos\theta-\cos^3\theta}{3\sin^3\theta}. \tag{1-3}$$

When this depth exceeds the thickness of the film and reaches the film-substrate interface, natural holes will form and be subject to growth to initiate dewetting.

After the substrate-vapor interface is exposed and three-phase boundaries are formed, dewetting initiates, the film edges retract, and the holes grow by capillarity-driven mass transport, which results from the chemical potential gradient as obtained from the Gibbs-Thomson equation [6] for surfaces with isotropic energies:

$$\mu = \mu^0 + \kappa\gamma_{fv}\Omega, \tag{1-4}$$

where μ^0 is the chemical potential for a zero-curvature surface, κ the local surface curvature, γ_{fv} the surface energy, and Ω the atomic volume. Surfaces with different local curvatures have different chemical potentials, and therefore material flows between the regions of different local curvatures, given that atomic kinetics allows the motion.

For viscous thin films, there are two likely mechanisms of capillarity-driven mass transport: surface self-diffusion and evaporation-condensation [12]. If atoms transport via surface self-diffusion, the flux of atoms J_s can be expressed as [6]:

$$J_s = -\left(\frac{D_s\gamma_{fv}}{kT}\right)\nabla_s\kappa, \tag{1-5}$$

where D_s indicates the surface self-diffusivity, γ_{fv} the film surface energy, kT the thermal energy, and κ the local surface curvature. As can be seen in Equation (1-1), the atomic flux directs along

the surface in the surface self-diffusion kinetics. If atoms instead move by the evaporation-condensation mechanism, the atomic flux J_v is perpendicular to the surface and is given by [6]:

$$J_v = K(P^0 - P_{eq}(\kappa)) , \tag{1-6}$$

where K is the rate constant related to the evaporation-condensation kinetics, P^0 the vapor pressure of the ambient, and $P_{eq}(\kappa)$ the equilibrium vapor pressure at a region with a local curvature κ. Because the vapor pressures of the films are usually small in solid-state dewetting, it is generally accepted [13, 14] that the dominant mass transport mechanism for the solid-state dewetting of thin films is capillarity-driven surface self-diffusion.

1.1. Growth of Holes and Retraction of Edges in Polycrystalline Films

Polycrystalline films do not have a long-range ordered crystal structure, and thus, at size scales larger than those of individual grains, random dewetted structures are observed. Therefore, the shape of the natural holes is also not uniform, as illustrated in Figure 1-4 [15], and generally treated as circular for the purpose of modeling. Brandon and Bradshaw [15] studied this isotropic-like hole propagation and developed a model describing the rate of edge retraction with time by analyzing Equation (1-5), assuming the edge retraction leads to the accumulation of material near the edge and the edge retains a semicircular shape, as illustrated in Figure 1-5. In their model, the edge retraction distance x scales as:

$$x = K\frac{t^{2/5}}{h^{3/5}} , \tag{1-7}$$

where t is time, h the initial thickness of the film, and K a kinetic constant. The rate of edge retraction decreases with time because the flux of material away from the retracting edges leads to accumulation and thickening around the edges. This decrease in the local curvature near the retracting edges leads to a decrease in the driving force for mass transport, thereby decreasing the retraction rate.

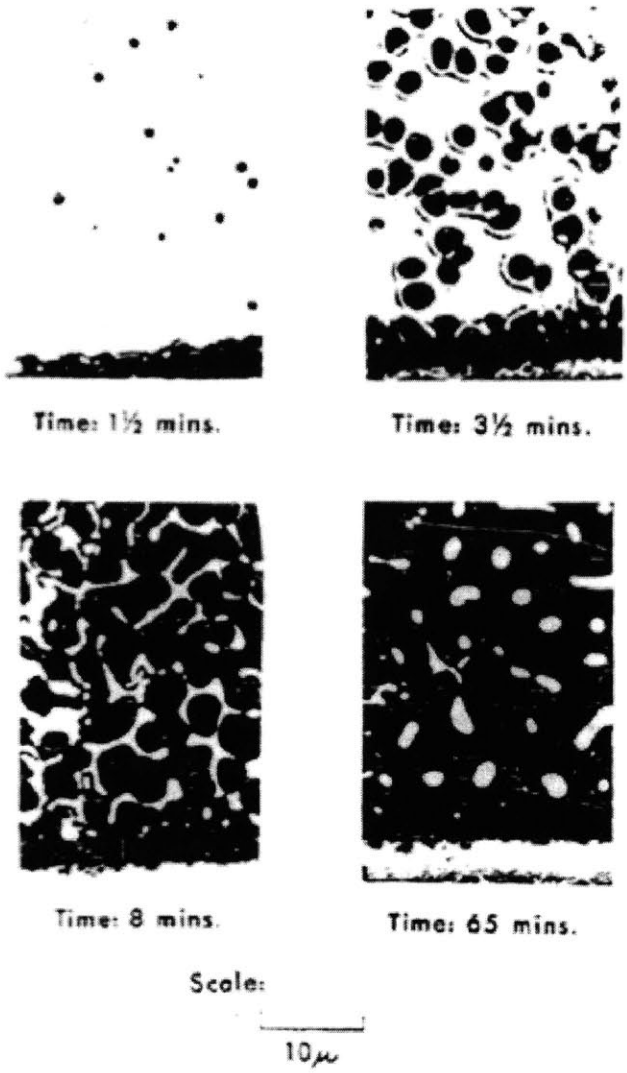

Figure 1-4. Optical micrographs of morphological evolution during solid-state dewetting of 110 nm-thick Ag films on mica substrates [15]. Black areas indicate natural holes. The film was annealed at 360 °C in air, for annealing times provided under the micrographs.

Similar models have been developed [14, 16, 17] by solving Equation (1-5) for isotropic γ_{fv} and applying different initial and boundary conditions. Although the details of the models vary, all share a power-law time dependence of the edge retraction rate.

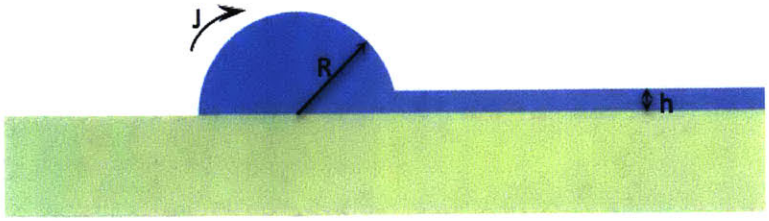

Figure 1-5. Retraction of edges and thickening of rims in the Brandon-Bradshaw model [15]. As the edges retract, capillarity-driven surface self-diffusion leads to material accumulation near the edges and the thickening rims retain the shape of a semicircle of radius *R*.

1.2. Growth of Holes and Retraction of Edges in Single Crystal Films

Although the absence of long range order in polycrystalline films often allows easier analysis and modeling of dewetting by assuming isotropic surface energies and surface self-diffusivities, because of inherent defects such as point defects, dislocations, and grain boundaries, it is very difficult to precisely control and predict how the films dewet. Using single crystal films, however, crystallographic constraints and anisotropy in energy and diffusivity allow much better control of the way the films dewet and reproducibility of the dewetted patterns. The dewetting phenomenologies discussed for polycrystalline films also occur in single crystal films in a much more regular and controllable way, giving a promising potential for dewetting to be used as a method of self-assembly.

Study of dewetting in single crystal films first arose when dealing with silicon-on-insulator (SOI) structures. Nuryadi et al. [18] observed that the growing natural holes in SOI structures dewet into arrays of islands that align to certain crystallographic orientations. Danielson et al. [19] also observed the similar hole propagation behavior. An illustration is given in Figure 1-6. The alignment of arrays occurs along the facets in SOI structures that minimize the total energy of the system. Because of anisotropy in the surface energy of Si, energy minimization can be achieved by exposing certain low energy facets.

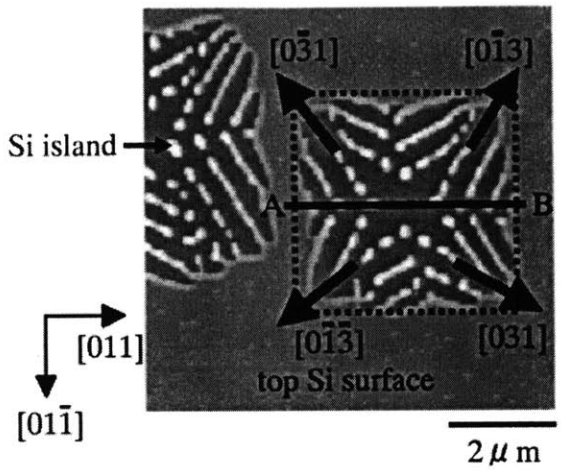

Figure 1-6. AFM image of the formation of ordered arrays of islands along certain crystallographic orientations in SOI structures (Si(100)), after Nuryadi et al [18].

Development of regular dewetting morphology has also been observed in other systems. Ye and Thompson [20] studied the propagation of natural holes in thin single crystal Ni films, and found that surface energy anisotropy of Ni films leads to a regular morphology of natural holes, as illustrated in Figure 1-7(a).

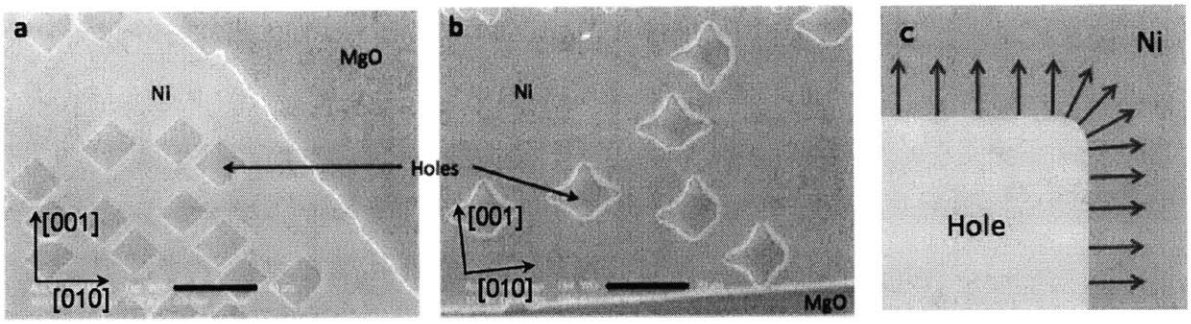

Figure 1-7. SEM images of natural holes in Ni(100) after annealing at 900°C under 2310 sccm reducing gas (5% H_2 95% N_2) conditions for **(a)** 3 hours and **(b)** 9 hours. Scale bars, 10 μm and 20 μm, respectively. As holes propagate, corners retract faster than edges, resulting in unstable growth at corners. **(c)** Such a corner instability can be understood in terms of difference in the size of the diffusion fields at a corner and an edge.

In the later stage of natural hole propagation, the corners of holes are observed to retract faster than the edges [20], as shown in Figure 1-7(b). This is understood in terms of the difference in the size of the diffusion fields at the corners and at the edges (Figure 1-7(c)). Because the corners have more area for atoms to diffuse into than the edges, for which material can diffuse only in the direction of the edge normal, corners have less rim thickening, leading to larger retraction velocities.

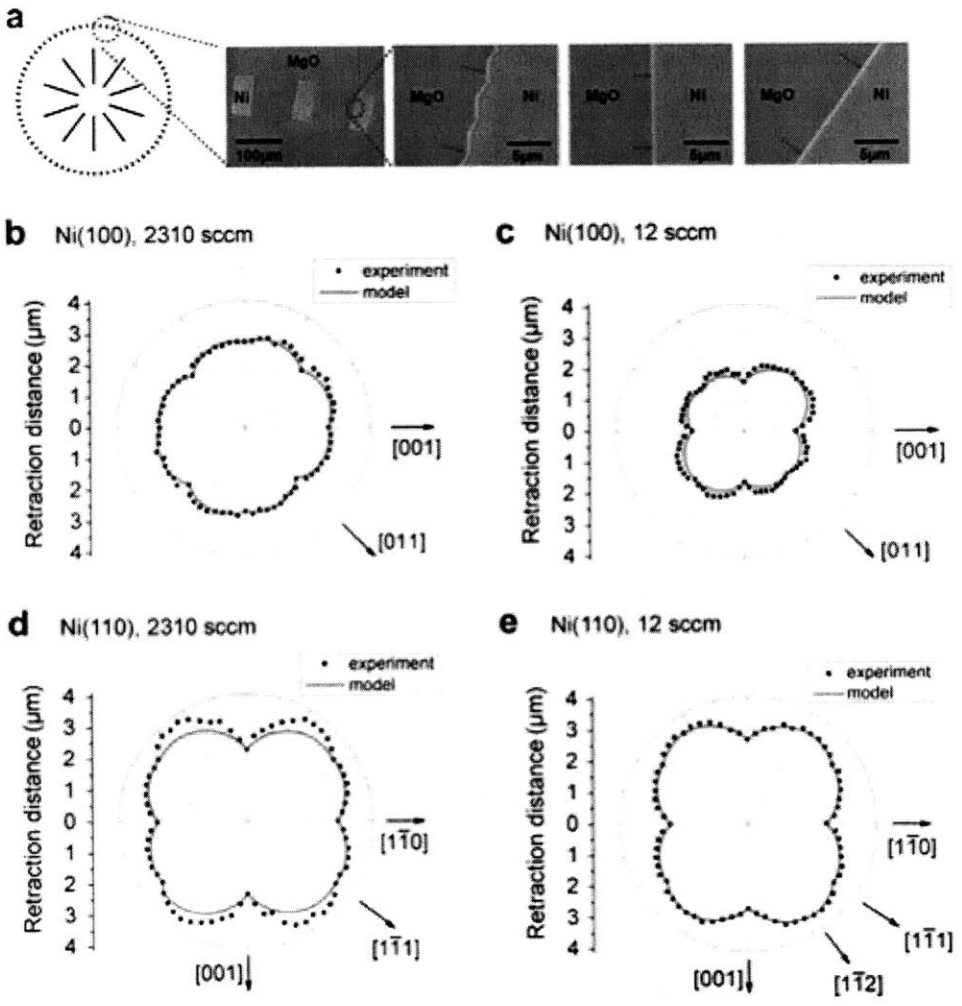

Figure 1-8. Anisotropic edge retraction velocities [21]. **(a)** Development of kinetically stable facets by a faceting instability. **(b)-(e)** Kinetic Wulff plots of the edge retraction distances after 318-minute anneals. Film orientation and flow rate of 5% H_2 95% N_2 reducing gas are indicated in each plot.

Because of anisotropy in surface energies and surface self-diffusivities, retraction of edges in single crystal films is anisotropic, which also explains the anisotropic shape of natural holes in such films. This anisotropy in the retraction rate is closely tied to the kinetic stability of edges in different crystallographic orientations, and Ye and Thompson [21] showed that such retraction rate anisotropy can be plotted to generate a kinetic Wulff plot as shown in Figure 1-8, which resembles an equilibrium Wulff plot showing surface energy anisotropy. Also, they showed that there exists a set of kinetically stable orientations corresponding to local cusps or minima in the kinetic Wulff plot, and the retraction rates in all other orientations can be successfully modeled by geometrically combining the retraction rates of these kinetically stable orientations, noting that all other edges in non-kinetically stable orientations undergo a faceting instability and develop combinations of kinetically stable facets (Figure 1-8(a)).

1.3. Modeling of Hole Growth and Edge Retraction in Single Crystal Films

Although many analytical models have been developed for isotropic dewetting, no simple analytical models thus far have been developed for edge retraction via dewetting in single crystal films because of anisotropic surface energies and diffusivities. Analysis of solid-state dewetting in single crystal films, therefore, usually requires development of numerical models and in many cases such models also require significant computational load.

Dornel et al. [17] conducted a numerical analysis of capillarity-driven edge retraction using a conventional anisotropic n-fold symmetric Wulff plot by numerically solving Equation (1-5) assuming the dominant mechanism of capillarity-driven mass transport is surface self-diffusion. However, they did not consider anisotropy in surface self-diffusivity which may also significantly affect the rate of edge retraction in anisotropic single crystal films.

As an alternative, the kinetic Monte Carlo (KMC) method has been used to simulate natural hole propagation in silicon-on-insulator (SOI) structures. Bussmann et al. [22] and Cheynis et al. [23] simulated the dynamics of dewetting in SOI systems and compared the result to the actual hole propagation morphology in SOI systems, as illustrated in Figure 1-9. However, because KMC simulations generally consider energetic relationships of atoms in a system with their adjoining atoms step-by-step, the computational load of such simulations exponentially

increases with increasing system size and therefore they generally cannot be used to analyze dewetting at a very large scale. The abovementioned work was conducted using a KMC simulation with three monolayers.

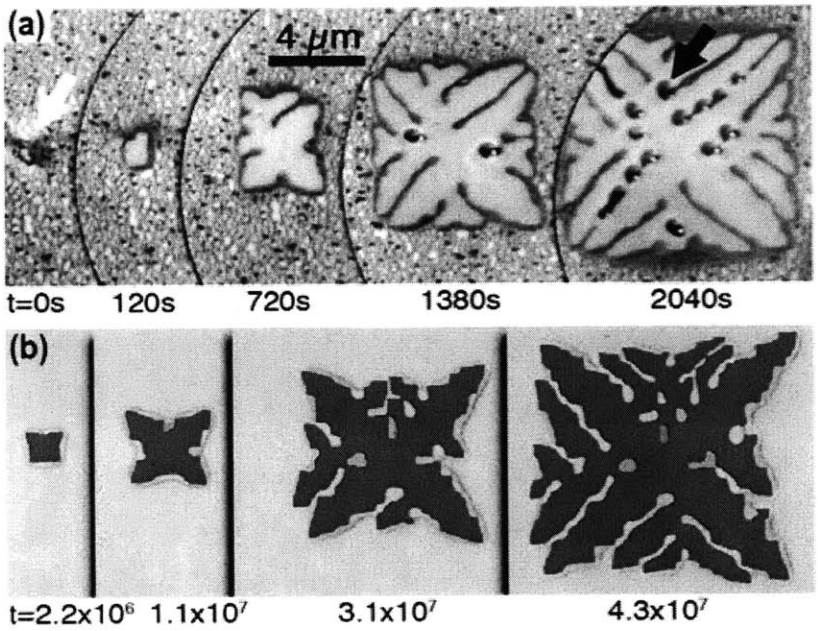

Figure 1-9. **(a)** LEEM images of dewetting of 22nm-thick SOI structures annealed at 870 °C [22]. **(b)** KMC simulation of dewetting with an initial film thickness of 3 layers [22]. Times after which the images were taken are provided under the images.

Carter et al. [24] studied morphological evolution of different structures using another computational method called the method of crystalline formulation. By assuming that the shape of interest is composed of facets appearing in the equilibrium Wulff shape and solving the diffusion equation on each facet rather than tracking individual atoms, they could significantly reduce the computational load arising from anisotropic surface energies and diffusivities. Along with successful description of dewetting morphologies in many different structures, they also could describe the differences that different capillarity-driven mass transport mechanisms [6], which are surface diffusion kinetics and evaporation-condensation kinetics, make during the morphological evolution of structures, as illustrated in Figure 1-10. A similar model has been

developed for the case of thin film structures to study solid-state dewetting in films with anisotropic surface energies and diffusivities [25].

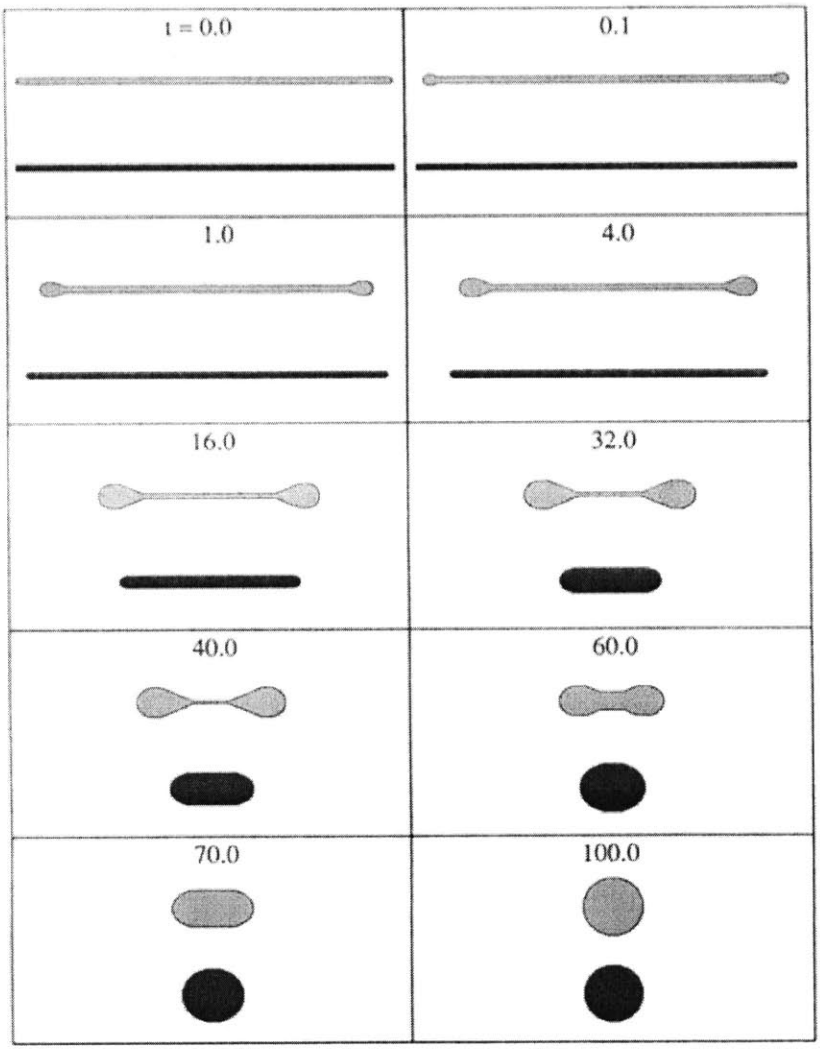

Figure 1-10. Time evolution of an elongated rectangle with a regular 16-gon Wulff shape [24]. The light gray structure evolves according to surface diffusion kinetics while the dark gray structure evolves by evaporation-condensation kinetics.

1.4. Templated Dewetting and Formation of Ordered Structures

As described previously, the absence of long range order in polycrystalline films and the random distribution of many different defects prohibit the formation of any long-range ordered

dewetting morphology in such films. However, dewetting in polycrystalline films has also been used to generate an ordered array of islands by either changing the substrate topography or pre-patterning the films and intentionally directing the mass transport flux to desired locations. One example is the study by Giermann and Thompson [26], in which they pre-patterned oxidized silicon substrates into a matrix of inverted pyramids. Upon deposition and dewetting of thin gold films, they found that under an appropriate pit spacing, pit size, and film thickness that allow the entire gold film to flow into the pits driven by the local curvature gradient, an ordered array of gold particles in the pits is observed, as illustrated in Figure 1-11.

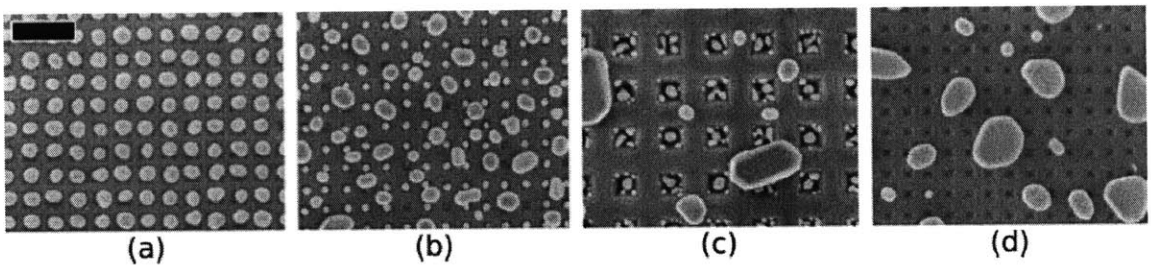

Figure 1-11. Formation of ordered arrays of Au particles by pre-patterning of oxidized Si substrates [26]. Under the appropriate pit spacing, size and film thickness, all of the deposited gold diffuses into the pits to form ordered arrays. Scale bar, 500 μm.

Pre-patterning the deposited film before dewetting is another way to generate ordered structures. Kim et al. [27] showed that polycrystalline Au films can also have an ordered dewetting morphology to some degree when the films are pre-patterned. Although the distribution of islands loses order when the initial pattern size becomes too large, they showed that in smaller patterns of order 10 μm, the number and the arrangement of islands formed after dewetting can be controlled by the aspect ratio and the size of the initial pattern, as illustrated in Figure 1-12. However, the degree of order obtainable in templated dewetting in polycrystalline films is limited because randomly distributed defects lead to random formation of natural holes that break the order imposed by templates at sufficiently large scales.

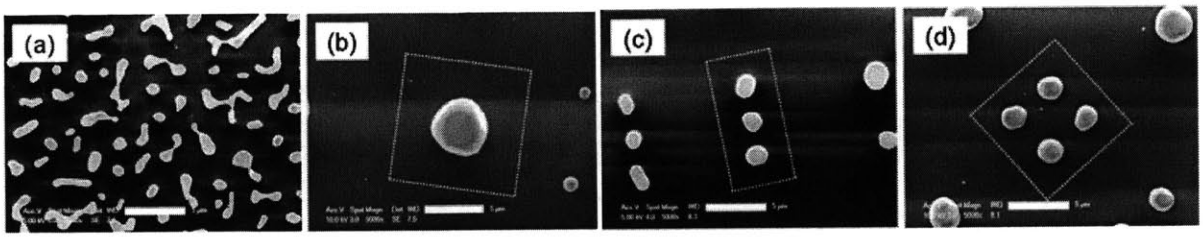

Figure 1-12. Formation of ordered Au islands by pre-patterning the gold film [27]. Unlike continuous films (**a**), patterned films can generate ordered arrays of islands in polycrystalline films (**b-d**), controlled by the aspect ratios of the initial pattern. Scale bars, 5 μm.

Because of their regular morphology as previously described, dewetting in single crystal films sheds a great potential for a self-assembly method. By properly pre-patterning the film, a number of different complex, regular dewetting morphologies which also are much smaller than the original patterns can be formed. Ye and Thompson [28] showed that pre-patterned Ni(100) and Ni(110) films can dewet to form complex ordered structures. Because the films have anisotropic surface energies and surface self-diffusivities, the dewetting morphology also depends on the initial orientation of the patterns. This is illustrated in Figure 1-13.

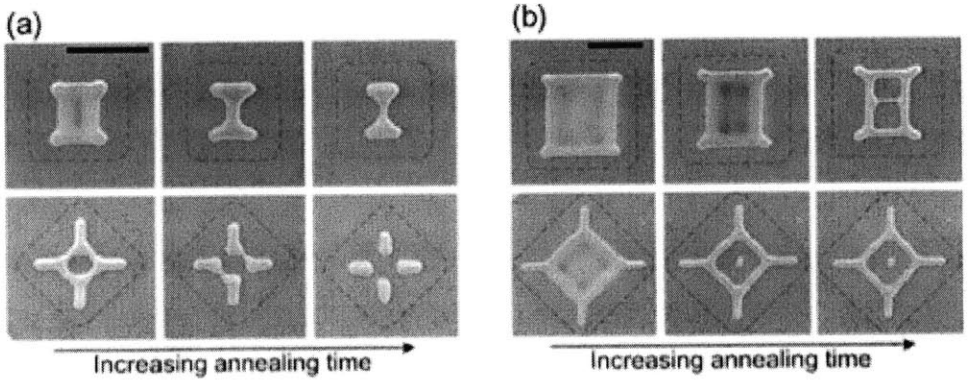

Figure 1-13. Dewetting of square patches patterned in a Ni(110) film [28]. Dewetting morphology is clearly dependent on the initial orientation and the size of the patches. Scale bars, 10 μm.

Thus far, insufficient data and inadequate models exist to thoroughly understand and predict the dewetting morphology of templated patterns. Therefore, more understanding of the

phenomenology along with the development of models to describe the process is crucial for solid-state dewetting of single crystal films to be used as an efficient self-assembly method.

Chapter 2. Objective of Thesis Research

Although many dewetting experiments have been conducted thus far to qualitatively study different dewetting phenomenologies, not much effort has been made to quantitatively study the behavior. Especially in single crystal films, anisotropy in surface energy and diffusivity leads to anisotropic dewetting behavior and therefore a detailed understanding of the effects of such anisotropy is critical for solid-state dewetting in single crystal films to be used in many possible applications such as cost effective patterning applications. This thesis research focuses on analysis and modeling of the most fundamental dewetting phenomenology, which is capillarity-driven retraction of edges, responsible for propagation of natural holes and introduction of later-stage dewetting phenomenologies. Providing a detailed quantitative analysis of anisotropic edge retraction behavior during capillarity-driven solid-state dewetting of single crystal films will serve as a starting point for further quantitative dewetting analysis and modeling.

This thesis is largely composed of two parts: experimental analysis of anisotropic edge retraction during solid-state dewetting and modeling of edge retraction using the method of crystalline formulation. By using single crystal Ni films on single crystal MgO as a model system, retraction of edges in kinetically stable orientations, which are defined as the orientations in which patterned edges remain straight during edge retraction, has been quantitatively measured and analyzed. Modeling of edge retraction has been conducted in collaboration with Rachel V. Zucker in Professor Carter's group in the MIT Department of Materials Science and Engineering using the crystalline formulation method originally developed by Carter et al. [24]. Because the system of interest is a thin film deposited on a substrate, a modified code was written in Mathematica to introduce substrates in the system.

Chapter 3. Experimental Methods

3.1. Film Deposition

Because it is known [29-31] that epitaxial Ni of different crystallographic orientations can be grown on MgO, single crystal Ni films deposited on polished single crystal MgO substrates were used as a model system. The films were deposited using a Balzers UMS500 electron-beam deposition system equipped with a turbomolecular pump and a mechanical pump. Because the system does not have a load-lock installed and thus the main chamber is exposed to the atmosphere when samples are loaded, a bake-out process was necessary to have enough desorption of gas molecules from the chamber wall. Before deposition, the chamber was baked at 120 °C and the substrates were heated at 320 °C for 24 hours. The Ni source was briefly heated for evaporation at a chamber temperature of 90 °C and substrate temperature of 270 °C before deposition, while the substrates were blocked from deposition flux, to increase purity of the source. The deposition was initiated at room temperature and at a base pressure of mid-10^{-8} torr and the pressure increased to low-10^{-7} torr during the deposition. The deposition rate was monitored with a quartz crystal deposition sensor.

3.2. X-ray Texture Analysis

Before subjecting the deposited films to dewetting at high temperatures, it was important to determine whether a satisfactory degree of epitaxy is achieved. X-ray texture analysis was used to determine both the out-of-plane and the in-plane orientations of the deposited Ni film. Because epitaxial films are highly textured, it was important to carefully calibrate the x-ray beam alignment with high-resolution angular steps to where the maximum diffraction occurs to correctly detect the diffraction peaks. Therefore, a Bruker HRXRD system in a 2θ-ω scan mode was used to confirm that the deposited film is epitaxial. Because a careful beam alignment is necessary, the actual scan was preceded by a series of detector scans (variation of 2θ), Z scans (variation of the normal position of sample), rocking curve scans (variation of ω), 2θ-ω scans (variation of both 2θ and ω), and χ scans (variation of tilt angle), to maximize the peak signal of

MgO. Different angles in the alignment procedures are illustrated in Figure 2-1. Ye [21] has previously reported that sometimes the deposited film may have a surface normal slightly off from that of the substrate, although the film is highly textured to have only one desired diffraction peak. This could also be detected by the HRXRD scan because the high-resolution steps allow determination of the tilt angle difference between the substrate and the film.

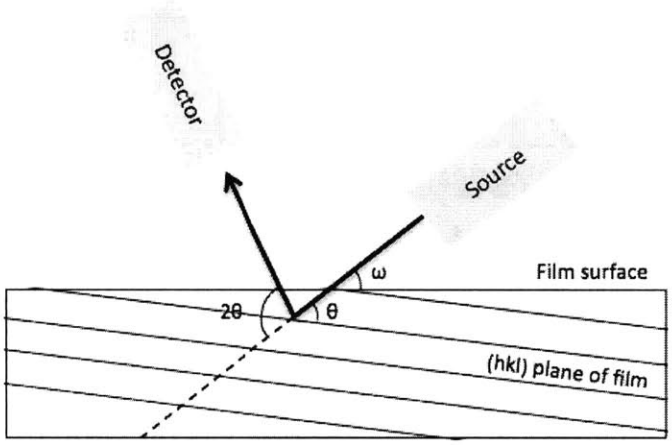

Figure 2-1. Schematic illustration of HRXRD scan settings. Each parameter was carefully adjusted to maximize signal from the epitaxial film.

In-plane orientation alignment of the film with the substrate was studied by using a Bruker D8 Discover system equipped with a 2D area detector. In this scan, 2θ can be properly centered to allow a simultaneous scan of (111) peaks in both MgO and Ni. When properly set, the system scans the sample to collect x-ray signal data for a range of rotation angles. Resulting pole figures can be analyzed to see if the in-plane alignment is satisfactory. Because of the crystallographic symmetry of the film, only a 180° rotation scan was enough to analyze in-plane alignment.

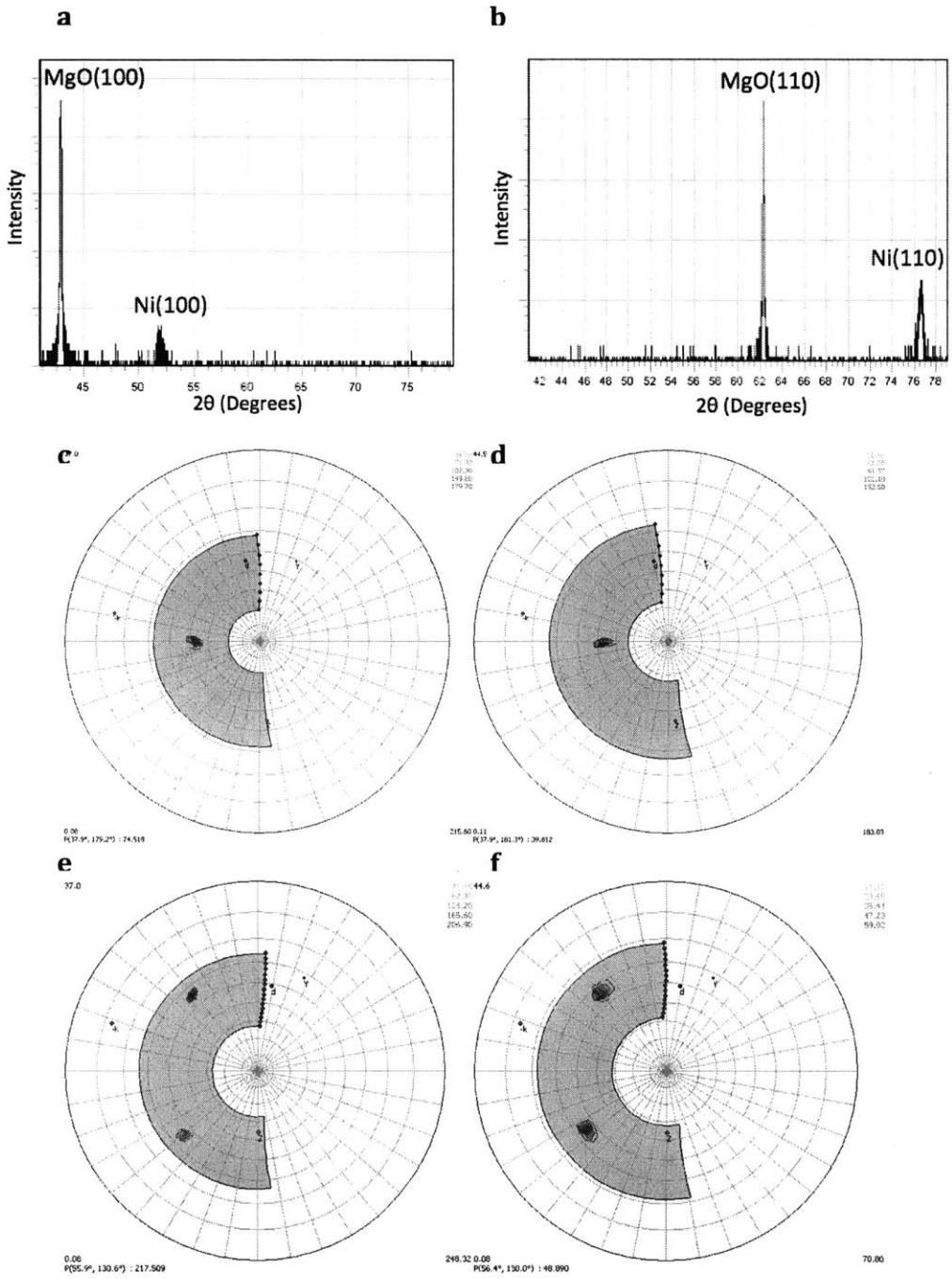

Figure 2-2. **(a)** 2θ-ω scan of Ni(100) film. **(b)** 2θ-ω scan of Ni(110) film. **(c)** (111) in-plane peak of MgO(100). **(d)** (111) in-plane peak of Ni(100) deposited on MgO(100). **(e)** (111) in-plane peak of MgO(110). **(f)** (111) in-plane peak of Ni(110) deposited on MgO(110).

Figure 2-2 illustrates the x-ray diffraction data for 130-nm thick Ni(100) and Ni(110) films, which were used in the study. Under the appropriate deposition conditions, the width of Ni peak was similar to the width of MgO substrate peak, which is an indication that a satisfactory level of out-of-plane and in-plane alignments was achieved.

3.3. Film Patterning

The as-deposited films were patterned by photolithography. After a dehydration step at 110 °C for 5 minutes on a hot plate, the sample was coated with OCG 825 positive photoresist at a spin rate of 3000 rpm for 30 seconds and baked again at 110 °C for 5 minutes to evaporate solvent. Followed by an alignment step and exposure to UV light, the photoresist was developed in OCG 934 1:1 developer and baked at 130 °C for 5 minutes. Following the wet etching of Ni in 69% HNO_3, H_2SO_4, CH_3COOH and H_2O with a volume ratio of 7.2 : 2 : 5 : 28, the remaining photoresist was first removed in acetone and then in ultrasonicated RR4 (dimethyl sulfoxide).

3.4. Thermal Annealing

To induce an appreciable degree of dewetting, a high temperature was required and therefore it was necessary to prevent oxidation of Ni by flowing a reducing gas (5% H_2 and 95% N_2). NiO can be reduced by hydrogen because oxidation of hydrogen to form water has a more negative energy of formation than that of Ni unless the temperature is far below 0°C [32]. A Lindberg/Blue quartz tube furnace with stainless steel flow tubes was used in which the flow rate of reducing gas is monitored and controlled by a rotameter installed between the gas inlet of the furnace tube and the gas cylinder.

3.5. Scanning Electron Microscopy

The morphology of dewetted films was usually observed by scanning electron microscopy. The imaging was carried out using an FEI/Phillips XL30 FEG ESEM. When Ni films are patterned and subject to dewetting, the exposed MgO surface is electrically insulating

and thus accumulates excess electrons to cause a charging effect in the image. This could be prevented by a low-vacuum mode in an environmental scanning electron microscope, in which water vapor is introduced in the chamber and the positively ionized water molecules neutralize the MgO surface. Although the image resolution was somewhat degraded due to a high pressure, the quality of the image generally was reasonably good for the purpose of the research.

3.6. Atomic Force Microscopy

When a more accurate surface profile was needed, atomic force microscopy was used. AFM imaging was done in tapping mode with a Veeco Nanoscope IV AFM. A standard tapping mode silicon probe was used. A high resolution imaging with a scan rate of approximately 0.2 Hz was conducted after a desired feature was located with high rate scans. It was important to decrease the actual scan rate during imaging because the probe generally did not retain a good contact with the surface at a high scan rate due to the large height of the dewetted features.

3.7. Focused Ion Beam Cross-Sections

A focused ion beam was used to make cross-sections of retracting rims in a Helios Dual Beam Workstation. Because MgO substrates are electrical insulators, significant charging develops with use of electron and ion beams. Therefore, the samples were preliminarily coated with 40 nm carbon. After cross-sectioning was complete, the samples were additionally coated with 20 nm carbon to coat the exposed cross-section to minimize charging in the image. This way, the charging effect in the image was minimized and reasonably good images could be obtained.

Chapter 4. Anisotropic Retraction of Patterned Edges in Thin Single Crystal Ni Films

As mentioned in previous chapters, more quantitative understanding of dewetting phenomena in single crystal films is needed to take advantage of templated dewetting. Also, results from experiments on templated dewetting of single crystal films can provide a basis for better general understanding of the effects of surface-energy and surface-diffusivity anisotropy on the capillarity-driven morphological evolution of thin films. In this chapter, the results from quantitative characterization and analysis of the retraction of pre-patterned edges with kinetically stable in-plane crystallographic orientations in single-crystal Ni(100) and Ni(110) films on single crystal MgO are reported.

4.1. Experimental Procedures

130 nm-thick single crystal Ni films were deposited on polished single crystal MgO substrates (purchased from MTI Corporation) using electron beam deposition. The as-deposited films were then patterned using optical photolithography with OCG 825 positive photoresist and OCG 934 1:1 developer followed by wet etching of Ni in 69% HNO_3, H_2SO_4, CH_3COOH and H_2O with a volume ratio of 7.2 : 2 : 5 : 28. The films were patterned into sufficiently large patches (200 μm long and 60 μm wide) so that no corner effects affected the experimental results. The patches were designed to align along kinetically stable retraction orientations, which are defined as the retraction orientations in which no in-plane faceting during edge retraction occurs. An illustration of the template pattern is given in Figure 4-1.

Annealing of the patterned films was conducted in a tube furnace at 900 °C with a reducing gas (5% H_2 and 95% N_2) flowing at a rate of 2310 sccm to remove nickel oxide from the Ni surface and prevent oxidation during edge retraction. Each annealing step was 3 hours long. In between the steps, edge retraction distances were measured up to a gross annealing time of 21 hours. Scanning electron microscopy using an FEI/Philips XL30 FEG ESEM was used for measurements of retraction distances in a low vacuum mode with a water vapor pressure of 0.9

torr. A focused ion beam (Helios Dual Beam Workstation) was used to make cross-sections for SEM imaging of the rims that form during edge retraction.

Figure 4-1. Illustration of the template pattern to be used in the experiment. The patches were designed to align along kinetically stable retraction orientations, which are defined as the retraction orientations in which no in-plane faceting during edge retraction occurs.

4.2. Results and Discussion

Using the same experimental conditions described above, Ye and Thompson [21] studied solid-state dewetting of single crystal Ni films that had been patterned into large patches with initially-straight edges aligned with different in-plane orientations. In some cases the edges remained straight as they retracted. These will be referred to as kinetically stable edges. Edges aligned to other orientations were subject to a faceting instability and developed an alternating row of kinetically stable facets. Figure 4-2 shows examples of a facetted edge and a kinetically stable edge.

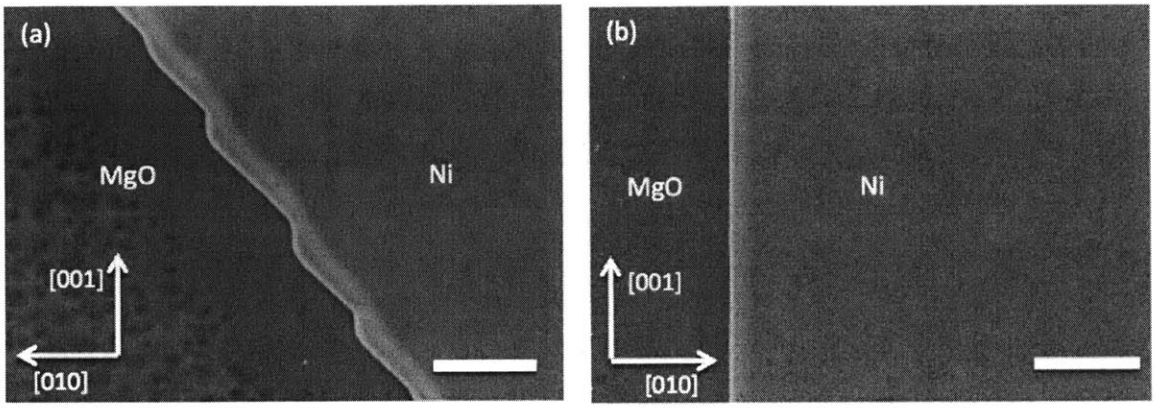

Figure 4-2. Edges in Ni(100) films after retracting during a 3-hour anneal at 900 °C under a reducing gas flow rate of 2330 sccm. In **(a)**, the original edge was straight and was aligned at a 35° rotation away from the in-plane [001] orientation. In this case the edge breaks up into kinetically stable in-plane facets. The edge aligned along the [001] direction in **(b)** is kinetically stable. The in-plane facets in **(a)** lie along [001] and [110] orientations, both of which are kinetically stable during retraction. Scale bars are 10 μm long.

Ye and Thompson [21] also showed that the rates of edge retraction in all in-plane crystallographic orientations can be successfully modeled using a geometric construction if the edge retraction rates of kinetically stable facets are known. In their analytical model, when the rates of edge retraction in kinetically stable orientations are known, the retraction rates in other orientations are given as [21]:

$$V(\theta) = V_1\left(\cos\theta - \frac{\sin\theta}{\tan\alpha}\right) + V_2\left(\frac{\sin\theta}{\sin\alpha}\right), \tag{4-1}$$

where V_1 and V_2 are velocities of the two alternating kinetically stable facets, θ the angle between the macroscopic in-plane orientation of the edge and that of facet 1, and α the acute angle between facets 1 and 2. The parameters of interest are illustrated in Figure 4-3.

For Ni(100) films, edges aligned to [100] and [110] in-plane directions were kinetically stable during retraction, and for Ni(110) films [001], $[1\bar{1}1]$ and $[1\bar{1}0]$ orientations were kinetically stable. In this chapter, more detailed analysis of the retraction kinetics during the shape evolution of these kinetically stable edges was made.

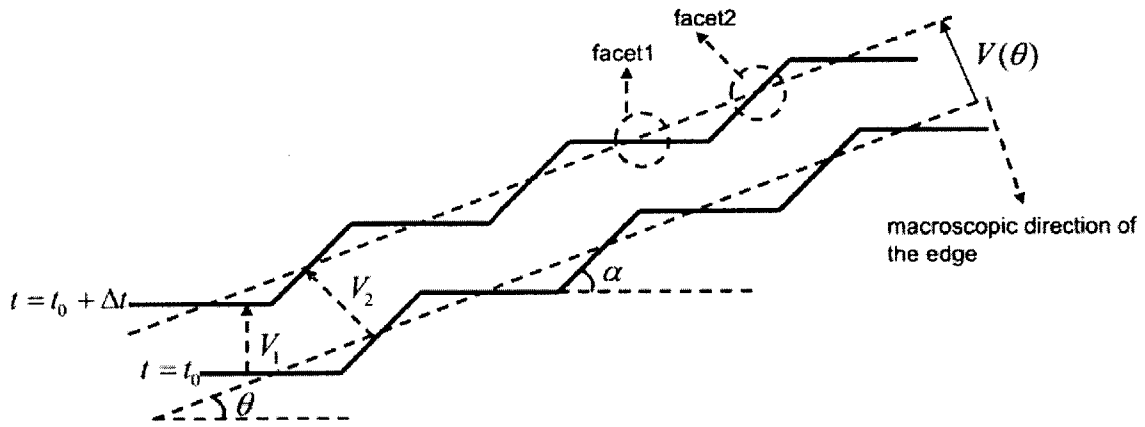

Figure 4-3. Schematic diagram of the edge retraction in non-kinetically stable orientations, after Ye and Thompson [21]. The dashed lines in the figure indicate the macroscopic orientation of the edge. During retraction, the edge becomes unstable and is decomposed into an alternating row of kinetically stable facets 1 and 2.

Figure 4-4 shows the retraction distance versus time for edges with kinetically stable orientations. The corresponding 2-dimensional equilibrium Winterbottom shapes, obtained by using *The Wulffmaker*, a program for equilibrium shape generation [33], are also provided except for the $[1\bar{1}1]$ orientation in Ni(110), where no simple 2-dimensional equilibrium shape is available because the equilibrium facet normals appearing in such a case are not in-plane with the retraction orientation.

As shown in Figure 4-4, the edge retraction rate is clearly anisotropic, and the rate of edge retraction decreases with time. Figure 4-5 shows images of cross-sections through edges after a period of retraction. As the edges retract, material accumulates at the edge to form a rim. While, in principle, an evaporation-condensation process can be responsible for the material transport that occurs during solid-state dewetting [16], it is generally accepted [13, 14, 19] that the dominant mass transport mechanism is capillarity-driven surface self-diffusion. This is supported by the development of rims on retracting edges, as the driving force for diffusion decreases as the curvature decreases ahead of the retracting edges. The increasing edge thickness results in a lower surface curvature and a lower curvature-driven atomic flux away from the triple line, so that the edge retraction rate decreases with time.

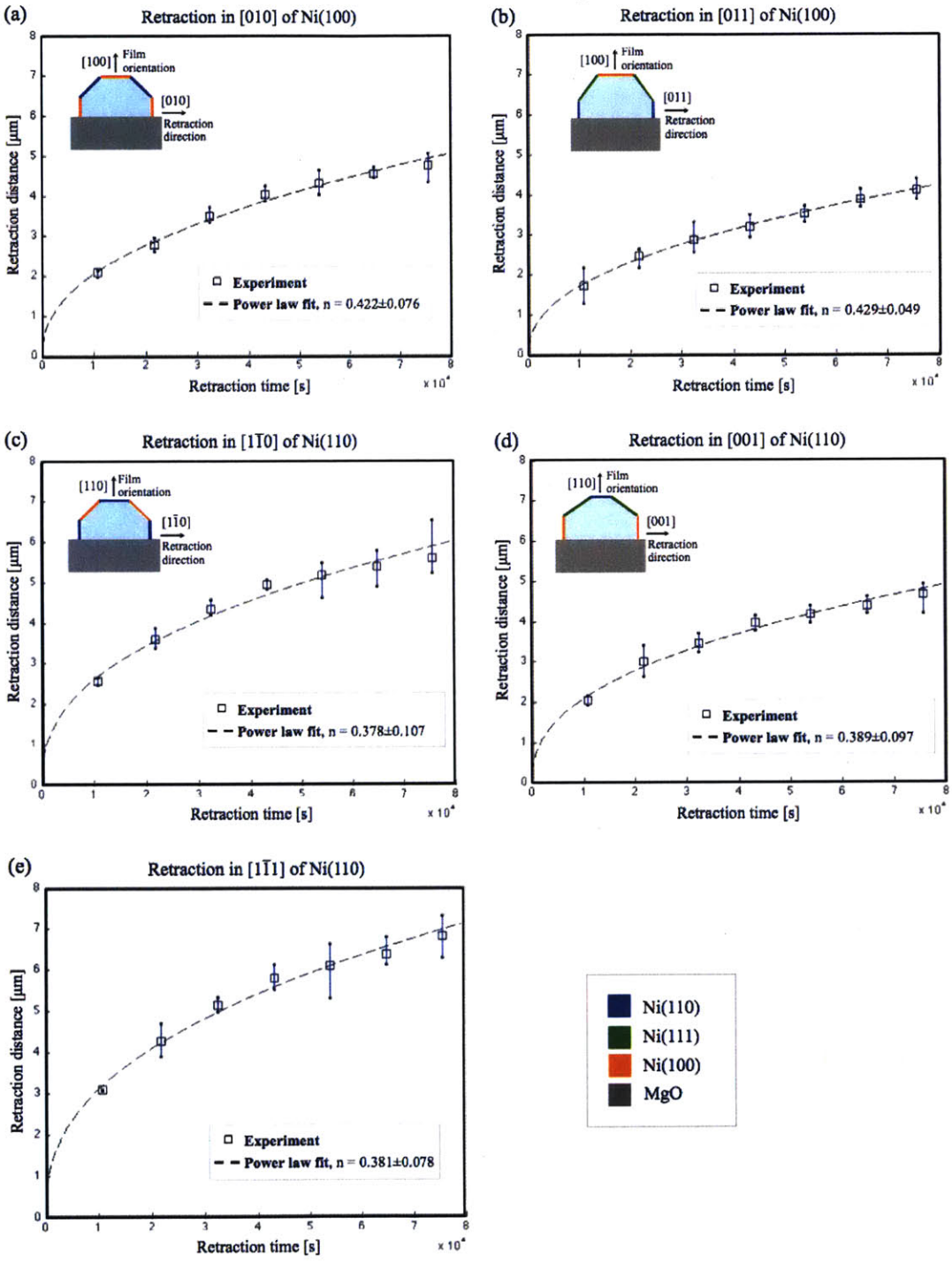

Figure 4-4. Retraction rates of kinetically stable edges for Ni(100) and Ni(110) films. The samples were annealed at 900 °C under a 2310 sccm reducing gas (5% H_2 95% N_2) flow. The exponents for power law fits are also given. Appropriate equilibrium Winterbottom shapes were obtained using *The Wulffmaker*, a program for equilibrium shape generation [33].

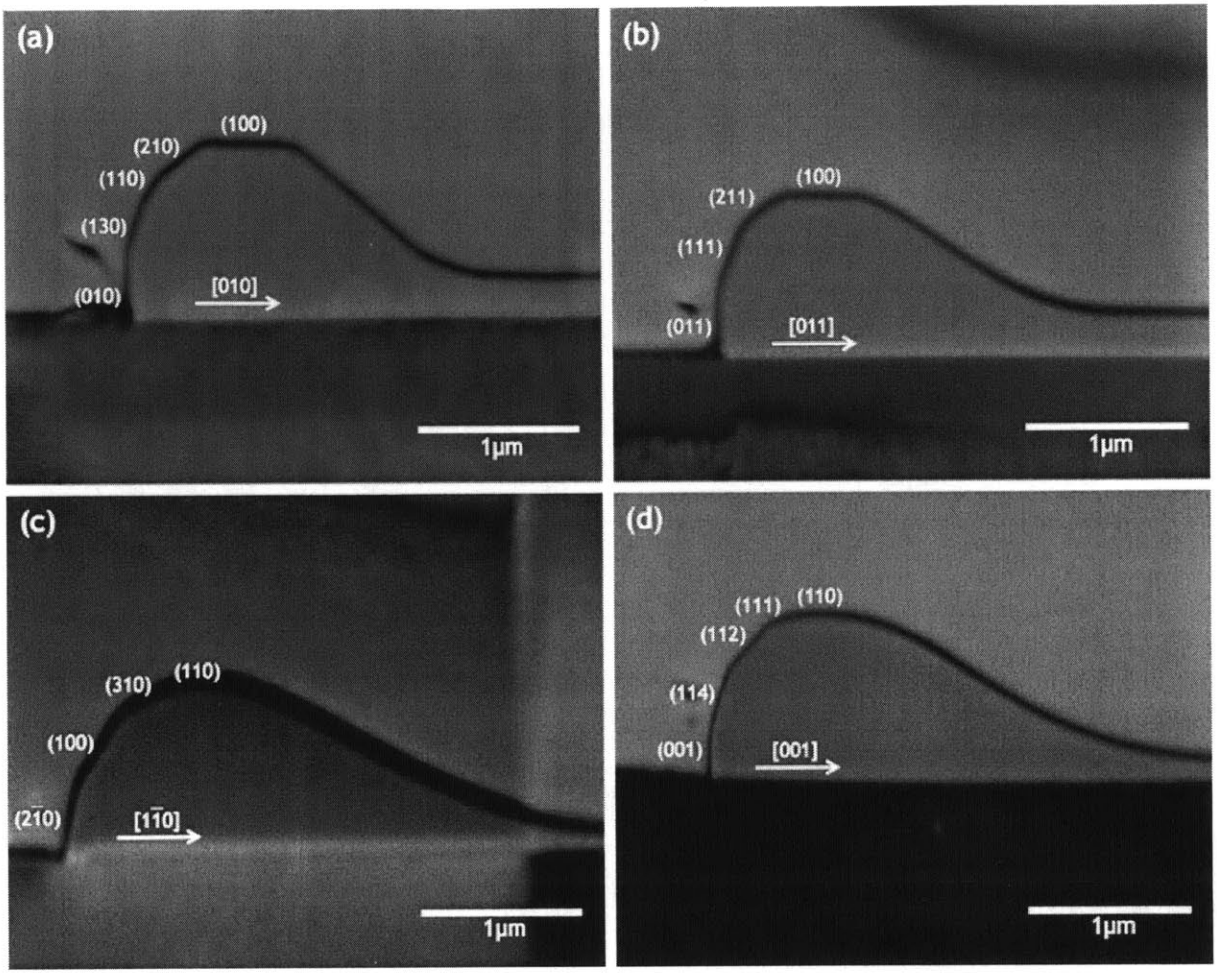

Figure 4-5. SEM images of the cross-sections of retracting edges in (**a**) and (**b**) Ni (100) films, and (**c**) and (**d**) Ni(110) films after 21-hour annealing at 900 °C. Retraction directions and facet planes are indicated. Scanning angle (angle between the electron beam and the cross section) is 52 degrees. Equilibrium facets comprising the Wulff shape of Ni appear, but some nonequilibrium facets also appear during retraction.

For surface self-diffusion in materials with isotropic energies and diffusivities, the surface atomic flux due to capillarity-driven surface self-diffusion is described by [6]:

$$J = -\left(\frac{D_s \gamma_{fv} N_s \Omega}{kT}\right) \nabla_s \kappa \ , \tag{4-2}$$

where D_s is the surface self-diffusivity, γ_{fv} the surface energy, N_s the number of atoms per unit area, Ω the atomic volume, k Boltzmann's constant, T the temperature, and κ the local surface

curvature. Numerical solutions [13, 14, 16, 19] of Equation (4-2) for isotropic surface energy and diffusivity have been provided by a number of authors. Wong et al. [14] found that a valley develops ahead of the rim and predicted that it would eventually touch the substrate and create two new triple lines. When this happens a line is left behind and a new rim forms at the new retracting edge. This phenomenon is called 'pinch-off'. Wong et al. also found that before pinch-off the edge displacement scales with time according to $x_o \propto t^{2/5}$. This is consistent with observed edge retraction in anisotropic single crystal Ni films, as seen in Figure 4-4 and Figure 4-6. While there is little variation in the power law exponent observed among the different crystallographic directions, given experimental error, the proportionality constant does vary among the different crystallographic directions.

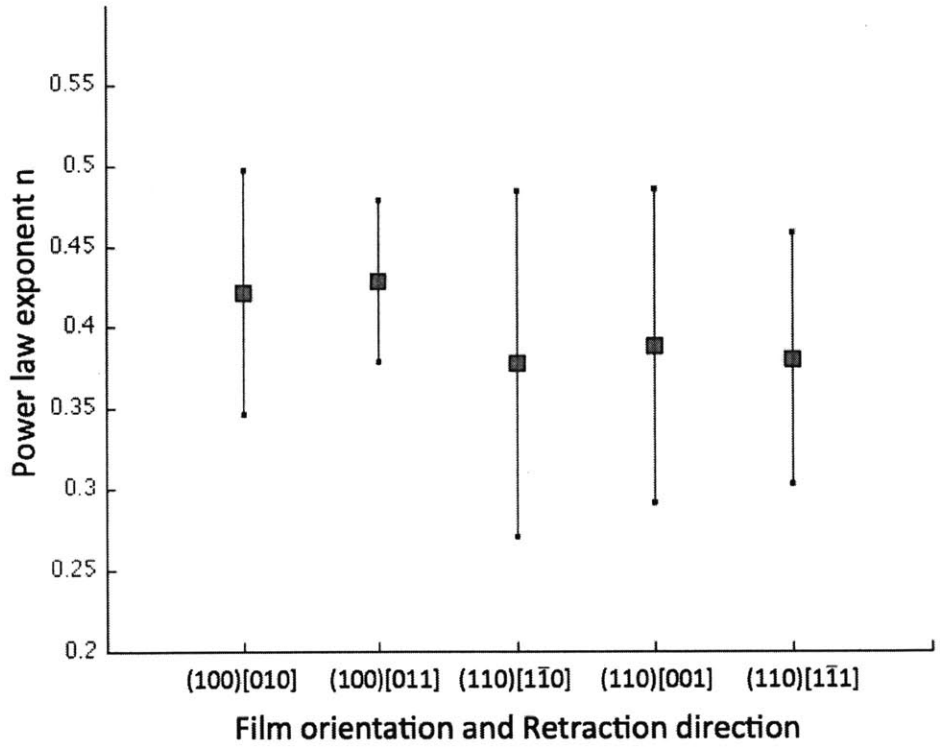

Figure 4-6. Power law fit exponents for experimental retraction data. Error bars of the exponents are constructed by calculating a 99% confidence interval using a t-distribution statistics multiplied by the standard error for the exponent.

Formation of natural holes in single crystal films leads to a regular hole morphology due to anisotropic surface energies and diffusivities. Ye and Thompson [21] studied this anisotropic behavior in natural hole formation, and found that in Ni(100), natural holes are bound by (011) facets and in Ni(110), they are bound by (001) and $(1\bar{1}0)$ facets when annealed at 900 °C under a 2310 sccm reducing gas (5% H_2 and 95% N_2) flow before they are subject to the later-stage dewetting instabilities such as corner instability, fingering instability, and pinch-off, as illustrated in Figure 4-7.

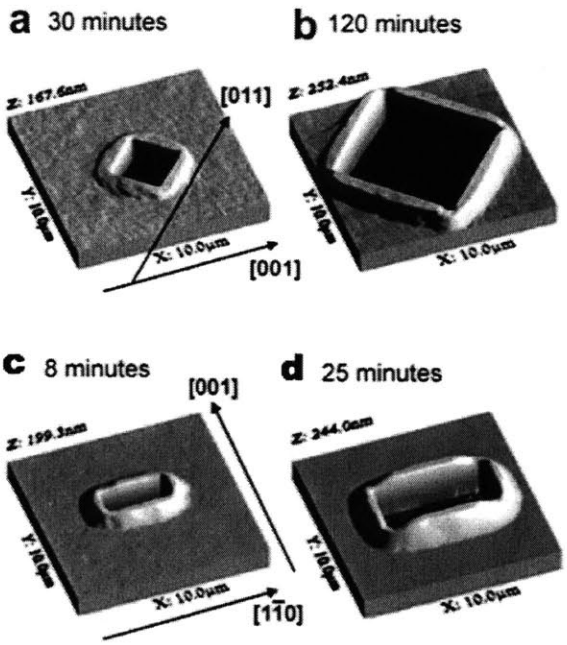

Figure 4-7. AFM images of growing natural holes in Ni(100) and Ni(110) films under 2310 sccm reducing gas condition, after Ye and Thompson [21]. The annealing times are indicated in the images. **(a)** and **(b)** Growth of natural holes in Ni(100). **(c)** and **(d)** Growth of natural holes in Ni(110).

This can be explained by the experimental result obtained in the experiment. Upon growth, natural holes are bound by the edges that retract the slowest. In Ni(100) films, the slowest retracting edges are [011] edges, as shown in Figure 4-4, while in Ni(110) films, the slowest retracting edges are [001] and $[1\bar{1}0]$ edges. In this case, although [001] edges retract the

slowest, they cannot close the hole shape by themselves and thus a perpendicular set of slow retracting facets is needed.

Although the anisotropic surface energies and diffusivities in different crystallographic orientations are readily available for Ni, developing an analytical model to predict the experimental results is very difficult, because the rates of edge retraction are determined by combinations of surface energies and diffusivities of different crystallographic planes appearing during the retraction of edges whose relative proportion also changes throughout the course of retraction until equilibrium is reached. Thus, to predict the rates of edge retraction, development of a numerical model is necessary, and this will be discussed in the next chapter.

4.3. Summary

Rates of edge retraction in kinetically stable orientations, which are defined as the orientations without faceting of edges during their retraction by capillarity-driven dewetting, were measured and analyzed. When the rates of edge retraction in kinetically stable orientations are known, the retraction rates in other orientations can be readily obtained by a simple geometric construction using the retraction rates of kinetically stable edges which are exposed during the retraction of non-kinetically stable edges.

The measurements were consistent with previous studies conducted under the same experimental conditions and have shown that the natural holes are bound by the slowest retracting edges before they are subject to further dewetting instabilities such as pinch-off, fingering instability, and corner instability, which further complicate the dewetting morphology in the later stage.

Although the measurement of edge retraction rates of kinetically stable edges allows the determination of retraction rates of other non-kinetically stable edges as previously illustrated, the prediction of edge retraction rates given anisotropic surface energies and diffusivities is also critical in quantitative analysis of dewetting, and this will be the topic of the next chapter, where a numerical model for prediction of edge retraction rates of kinetically stable edges is developed and analyzed.

Chapter 5. Numerical Model for Prediction of Retraction Rates of Kinetically Stable Edges

The evolution of shapes by capillarity-driven surface self-diffusion when the material of interest has anisotropic surface energies and diffusivities is generally analytically intractable due to its complexity [24]. However, development of a model capable of describing such shape evolution is critical in understanding of solid-state dewetting in thin single crystal films. In this chapter, a 2-dimensional numerical model to analyze and predict the capillarity-driven anisotropic edge retraction in kinetically stable orientations is developed. The model is able to deal with the retraction of edges when their equilibrium shapes can be made 2-dimensional; this is true when the equilibrium facet normals appearing in the Wulff shape are all in-plane with the retraction direction. The model was developed in collaboration with Rachel V. Zucker in Professor Carter Group in the Department of Materials Science and Engineering of Massachusetts Institute of Technology.

5.1. Development of the Model

Although many numerical simulations have been conducted to analyze dewetting of isotropic thin films, tracking the morphological evolution by diffusive transport is known to be very difficult in materials with anisotropic surface energies and diffusivities [24]. However, Carter et al. [24] used the method of crystalline formulation, in which all surfaces and interfaces are assumed to be completely faceted and bound only by facets appearing in the equilibrium Wulff shape in the entire course of morphological evolution, and greatly reduced the computational difficulties in tracking the morphological evolution in materials with anisotropic diffusivities and energies. In this model, the velocity of movement along each facet is kept uniform and driven by the weighted mean curvature κ, which, in the case of completely faceted shapes in 2-D, is defined simply as [24]:

$$\kappa = \frac{\sigma \Lambda(n)}{L} = \frac{\int_0^L \mu(s,t)ds}{L}, \tag{5-1}$$

because

$$\Delta E = \kappa_i L_i dx = dx \int_0^{L_i} \mu_i(s) ds, \tag{5-2}$$

where σ is the convexity factor determined from the geometric relationship of a facet with its adjacent facets, $\Lambda(n)$ the length of the facet in the Wulff shape, L the facet length, μ the chemical potential of the facet, and s the coordinate along the facet. Subscript i indicates a specific facet in the shape of interest. An illustration of calculating the convexity factor is provided in Figure 5-1. For 2-dimensional shapes, the convexity factor is +1 when the relationship of the facet with its adjacent facets is convex, -1 when it is concave, and 0 otherwise.

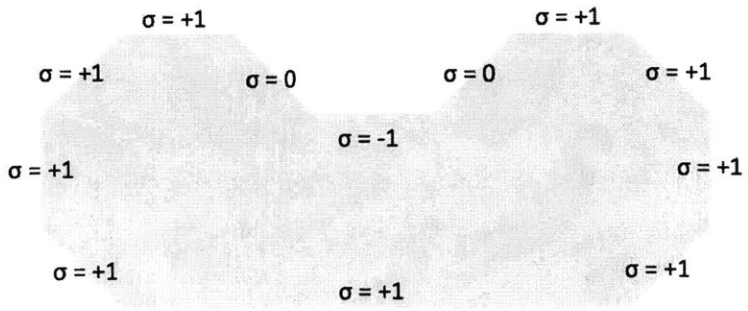

Figure 5-1. Illustration of convexity factor calculation. Convexity factors in 2-dimensional shapes are determined by the relationship of the facet of interest with its adjacent facets.

By solving the flux equation with Equation (5-1) with the continuity condition of the chemical potential and the flux at corners, the evolution of shapes by capillarity-driven diffusion can be simulated. For surface diffusion kinetics,

$$v_i(t) = -\frac{\delta}{\delta s} J_i(s,t) \neq f(s) \tag{5-3}$$

and

$$J_i(s,t) = -D_i \frac{\delta}{\delta s} \mu_i(s,t)\,. \tag{5-4}$$

Equation (5-3) is a critical assumption in the model. By construction, each facet in the shape of interest should move in a uniform velocity. The velocity of each facet is not a function of the coordinate along the facet. Therefore, combining Equations (5-3) and (5-4),

$$\mu_i(s,t) = \mu_i - \frac{J_i}{D_i}s + \frac{v_i}{2D_i}s^2 \,. \tag{5-5}$$

Boundary conditions for Equation (5-5) can be obtained by imposing a continuity requirement at the corners. The chemical potential and the flux have to be continuous at the corners where two facets meet:

$$\mu_i(s,t) = \mu_i - \frac{J_i}{D_i}L_i + \frac{v_i}{2D_i}L_i^2 \tag{5-6}$$

and

$$J_{i+1} = J_i - v_i L_i \,. \tag{5-7}$$

Equation (5-1) can now be further expanded using these conditions:

$$v_i = \frac{6D_i(\kappa_i - \mu_i) + 3J_i L_i}{L_i^2} \,. \tag{5-8}$$

Because the velocity along each facet should be uniform by construction, topological changes are made by inserting infinitesimal steps into the places where such an insertion does not violate any stability laws. From Equation (5-1), it can be seen that only a facet with convexity factor σ of 0 can be inserted because the chemical potential approaches infinity for infinitesimal steps of nonzero σ. Also, steps of $\sigma = 0$ can be inserted where the chemical potential is zero. After steps are inserted at such locations, each step is tested for stability. When the step satisfies the stability criteria, it further grows to form another facet, while it will shrink and disappear if it does not meet the criteria. One criterion is that after step insertion, two newly formed adjacent facets should satisfy the definition of weighted mean curvature:

$$\kappa_{s-1} = \frac{\int_0^{cL}\mu(s,t)ds}{cL} \tag{5-9}$$

and

$$\kappa_{s+1} = \frac{\int_{cL}^{L}\mu(s,t)ds}{(1-c)L} \,, \tag{5-10}$$

where c indicates the location of the step along the facet coordinate s. Another criterion is imposed to ensure that the step grows:

$$\sigma_{s-1}\int_0^{cL}\mu(s,t)ds > \Lambda(n_{s-1})\ . \qquad (5\text{-}11)$$

Additionally, the model assumes local equilibrium throughout the course of morphological evolution. Therefore, the adjacent facets of each facet in the shape should also be the adjacent facets in the equilibrium Wulff shape.

The original simulation constructed by Carter et al. dealt with free-standing 2-dimensional structures. Therefore, it is necessary to introduce the substrate-film interface to successfully simulate the morphological evolution during edge retraction. This can be done using the Winterbottom construction [9]. As illustrated in Figure 1-2, the equilibrium Winterbottom shape is determined by the conventional Wulff-Herring construction [7], but the surface energy of the facet adjoining the substrate-film interface is decreased by the adhesion energy of the interface. A similar model has been independently developed by Klinger et al.[25] for analysis of dewetting of thin films with high anisotropy. In their model, the analysis was carried out analytically for a single edge, retracting in the $[11\bar{2}]$ direction of a Au(111) film, where only two facets were considered: (111) and (100). In this thesis, such an analysis is expanded and applied to many different orientations with different facets.

Because the simulation is two-dimensional, shapes bound only by the facets perpendicular to the two-dimensional plane of interest can be treated. Although the $[1\bar{1}1]$ orientation of Ni(110) is a kinetically stable orientation, the two-dimensional Wulff shape for this edge retraction situation is not bound only by the facets perpendicular to the two-dimensional plane and therefore the orientation could not be simulated.

Using the readily available equilibrium shape of nickel [34, 35], surface self-diffusivities [36, 37], Ni surface energies [38, 39] and Ni-MgO adhesion energies [40, 41], edge retraction rates of kinetically stable edges in Ni(100) and Ni(110) films were calculated for comparison with experimental results. As surface self-diffusivities are generally several orders of magnitude larger than interfacial self-diffusivities [6], the self-diffusivity at the interface was set to be 10^{-3} when normalized by the diffusivity on (110) planes in the $[1\bar{1}0]$. When the oxygen concentration is sufficiently low under a sufficient level of reducing gas (5% H_2 and 95% N_2), the equilibrium shape of Ni is known to resemble that of Lennard-Jonesium, composed of (100), (110), and (111) facets [34, 35]. Using the available data provided in Table 5-1 and Table 5-2, the equilibrium

Winterbottom shape in each case of edge retraction is constructed as shown in Figure 5-2 by using *The Wulffmaker*, a program for equilibrium shape generation [33].

Surface and Orientation	D_0 ($cm^2\ s^{-1}$)	Q (eV)	D(T = 900 °C) ($cm^2\ s^{-1}$)
(100)	2.6 ± 1.6	1.54 ± 0.07	6.3×10^{-7}
(110)[001]	12.8 ± 4	1.74 ± 0.04	4.34×10^{-7}
(110)[1$\bar{1}$0]	23.9 ± 6.4	1.85 ± 0.04	2.73×10^{-7}
(111)	0.0005 ± 0.0003	0.62 ± 0.08	1×10^{-6}

Table 5-1. Surface self-diffusivities of Ni [36, 37]. Following the Arrhenius relationship, the diffusivity $D = D_0 e^{-\frac{Q}{kT}}$ where k is Boltzmann's constant and T is the temperature of interest. (100) and (111) planes have isotropic diffusivities.

Crystallographic Surface	Ni Surface Energy (J/m^2)	Ni-MgO Adhesion Energy (J/m^2)
(100)	2.0 ± 0.2	1.12
(110)	2.03 ± 0.2	1.92
(111)	1.96 ± 0.2	-

Table 5-2. Ni surface energies [38, 39] and Ni-MgO adhesion energies [40, 41] for different crystallographic planes. When epitaxially grown, Ni(100) grows on MgO(100) and Ni(110) grows on MgO(110).

All parameters were determined from readily available data and no adjusting parameters were used. As can be seen in Figure 5-3, the simulation successfully predicts the local thickening of the retracting edge until the two thickening rims merge together to form the equilibrium Winterbottom shape upon completion of dewetting.

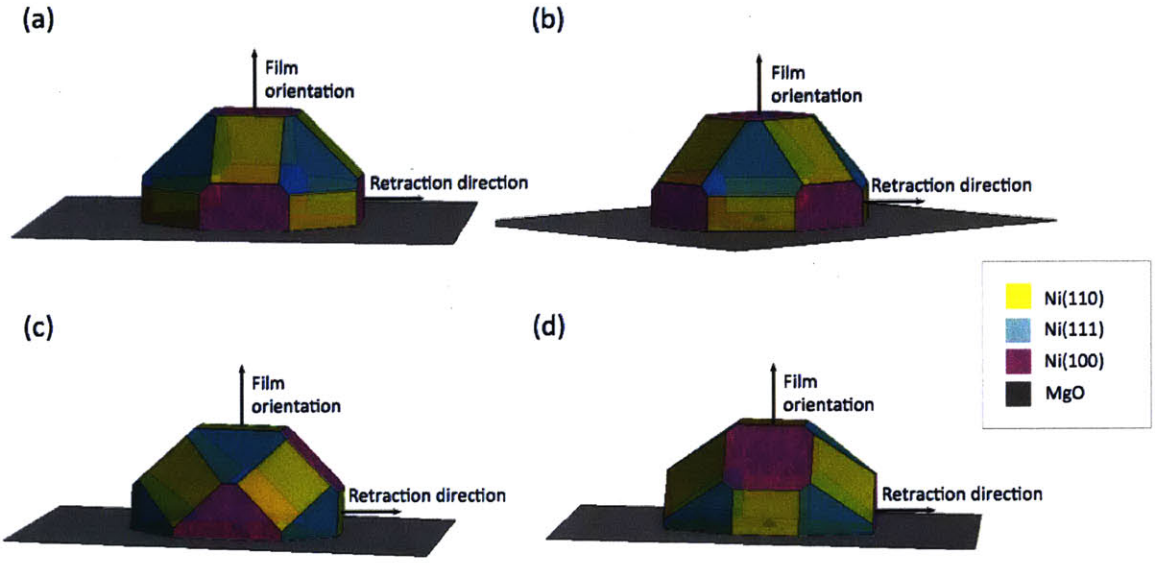

Figure 5-2. Equilibrium Winterbottom shapes. **(a)** Winterbottom shape for patches in Ni(100) retracting in [010]. **(b)** Winterbottom shape for patches in Ni(100) retracting in [011]. **(c)** Winterbottom shape for patches in Ni(110) retracting in $[1\bar{1}0]$. **(d)** Winterbottom shape for patches in Ni(110) retracting in [001]. The equilibrium shapes were generated using *The Wulffmaker*, a program for equilibrium shape generation [33].

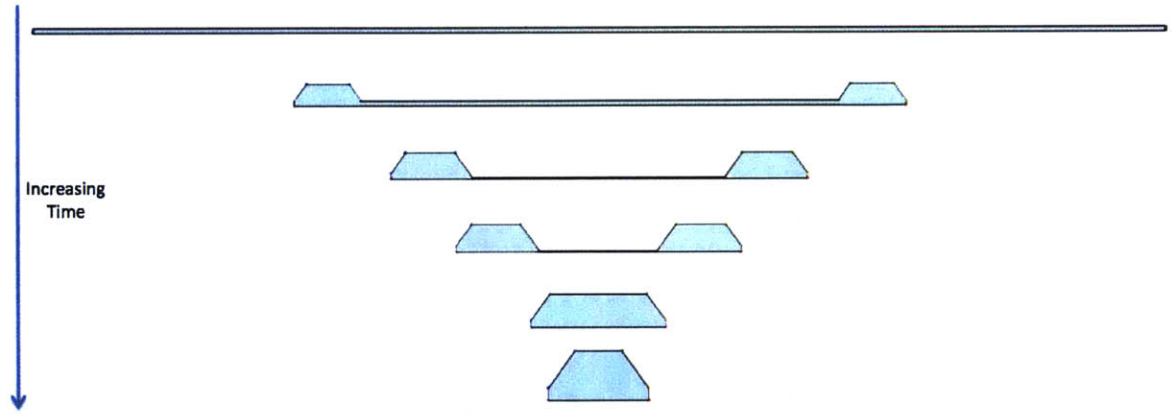

Figure 5-3. 2-D simulation of the morphological evolution of retracting edges in a cross-section of a Ni(100) strip, with edge retraction in the [011] in-plane direction. The strip is initially 40 μm wide and 130 nm thick. The retracting edges locally thicken and merge in the later stage to form an island/line with the 2-D equilibrium Winterbottom shape.

5.2. Limitation of Model

As previously mentioned, edge retraction in the $[1\bar{1}1]$ direction in Ni(110) films cannot be simulated because the facet normals appearing during the retraction are not in-plane with the retraction orientation and therefore cannot be treated as a 2-dimensional phenomenon. To deal with such orientations, development of a 3-dimensional model is necessary, but such a model is much more difficult to develop. Aside from obvious increase in the number of facets comprising a 3-dimensional structure, one key factor making the development of a 3-dimensional model difficult results from the calculation of weighted mean curvature. In 3-D, the weighted mean curvature of a facet S_i in completely faceted shapes is [42]:

$$wmc(S_i) = -\frac{1}{A(S_i)}\sum \delta_{ij} f_{ij} l_{ij} \ , \tag{5-12}$$

where A is the facet area, δ the convexity factor for an edge ij, f the factor related to the Wulff shape, and l the length of the edge ij. The 3-D simulation requires calculation of weighted mean curvature with all existing edges and thus is more complicated.

Another difficulty in the 3-dimensional model development arises from the criterion for step formation [43]. In 3-dimensional structures, more than 3 kinds of steps are possible and more than one step can form on a facet at the same time. Therefore, much more complicated criteria for stepping than those used in the 2-dimensional model need to be developed, because simply ignoring the possibility of step formation or randomly choosing the locations for stepping at each time step may lead to a significant error.

5.3. Summary

In this chapter, a 2-dimensional model capable of dealing with edge retraction in kinetically stable orientations was developed using the method of crystalline formulation developed by Carter et al. [24] and modified to introduce substrates in collaboration with Rachel V. Zucker in Professor Carter Group in MIT DMSE. By assuming that the shape of interest is completely faceted throughout the course of morphological evolution and that only equilibrium

facets satisfying the local equilibrium condition appear, the computational load could be significantly lowered.

Although the nature of 2-dimensional structures limits its use to the cases where the retracting edges can be treated as 2-dimensional structures by only having facets whose normals are in-plane with the retraction direction, it still provides a useful prediction and explanation of the edge retraction and captures the physics of rim formation during retraction. Quantitative data were also obtained using the model and will be presented in the next chapter along with the experimental data.

Because the model can only handle 2-dimensional structures, edge retraction in the $[1\bar{1}1]$ direction of Ni(110) films cannot be simulated because the equilibrium shape in this case cannot be treated as 2-dimensional. Such a limitation can be overcome by developing a 3-dimensional crystalline formulation model, but development of such a model is much more difficult because of heavy computational load and requirement of new stepping criteria.

Chapter 6. Comparison of Experiment and Model

In this chapter, the experimental results and the modeling results discussed in the previous chapters are compared and analyzed. When there is a disagreement between the model and the experiment, possible explanations for the disagreement are also provided. Surface self-diffusivity and surface energy values used in the model contain a range of error that can affect the result significantly. The modeling results are adjusted by changing the surface self-diffusivities within the range of error. Existence of nonequilibrium facets and formation of local valleys behind the retracting rims can also be possible sources of error. Other possible sources of error include the fact that the actual edges are not fully facetted and that it takes a finite length of time to have rim faceting.

6.1. Experimental and Modeling Data

Figure 6-1 presents the experimental data and the modeling prediction on the same plot for each of the kinetically stable facets studied. Although the model predicts the experimental result in the correct order of magnitude in all cases, there still is a significant degree of disagreement between the experimental data and the modeling data in some orientations. It should also be noted that due to the limitation of the 2-dimensional model, no prediction for the edge retraction in the $[1\bar{1}1]$ direction of Ni(110) films could be made.

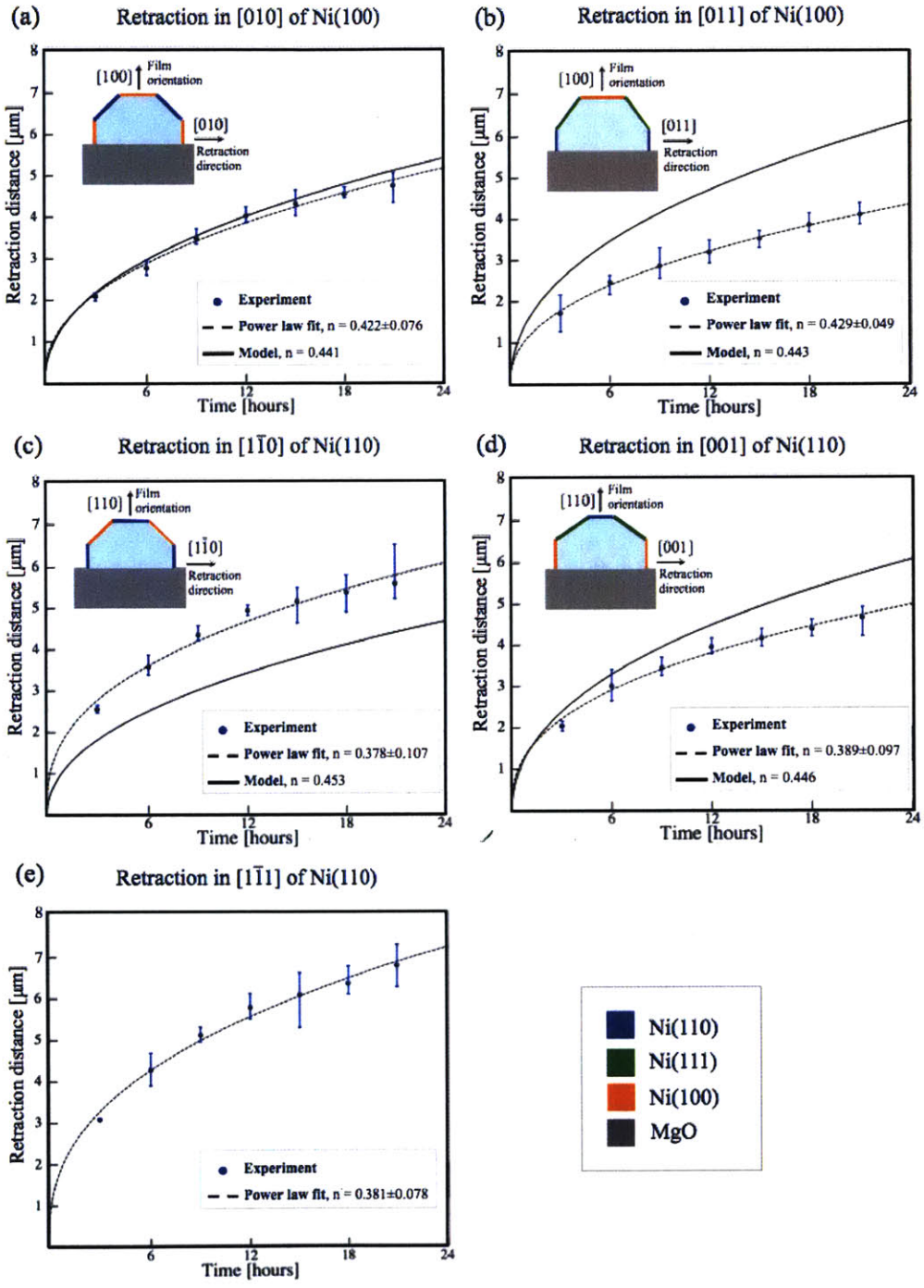

Figure 6-1. Experimental and model retraction rates of kinetically stable edges for Ni(100) and Ni(110) films. The samples were annealed at 900 °C under a 2310 sccm reducing gas (5% H_2 95% N_2) flow. The exponents for power law fits are also given. Appropriate equilibrium Winterbottom shapes were obtained using *The Wulffmaker*, a program for equilibrium shape generation [33].

As shown in Table 5-1 and Table 5-2, the surface self-diffusivity data obtained from literature [36, 37] contains significant ranges of error, while the ranges of error in energy are comparatively small [38, 39]. Changing the energy within the given ranges of error generally did not change the retraction rate significantly. As shown in Figure 6-2 and Figure 6-3, although the ranges of error were at most 10% for each surface energy, changing the energy of a facet in each equilibrium shape by 10% led to a change of at most 13% in the retraction rate.

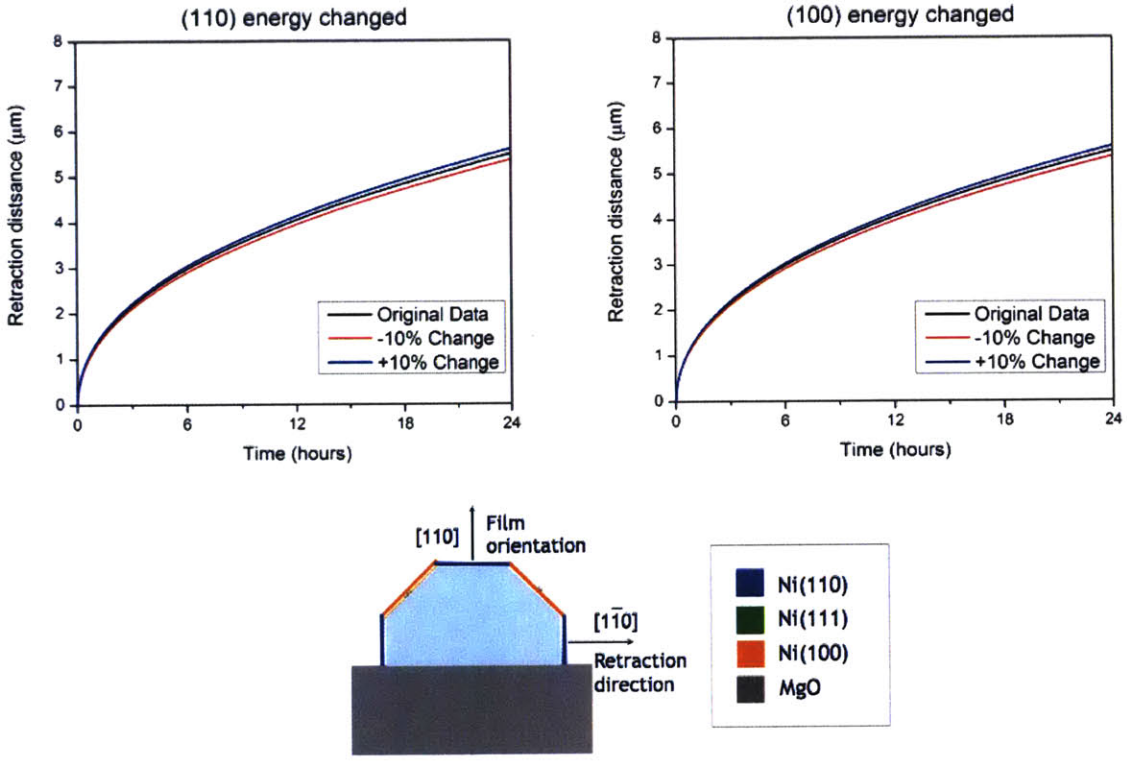

Figure 6-2. Sensitivity of edge retraction rate with respect to surface energy in Ni(110) films. For the given equilibrium shape, the retraction rate was measured after changing the facet energy as indicated in the figure.

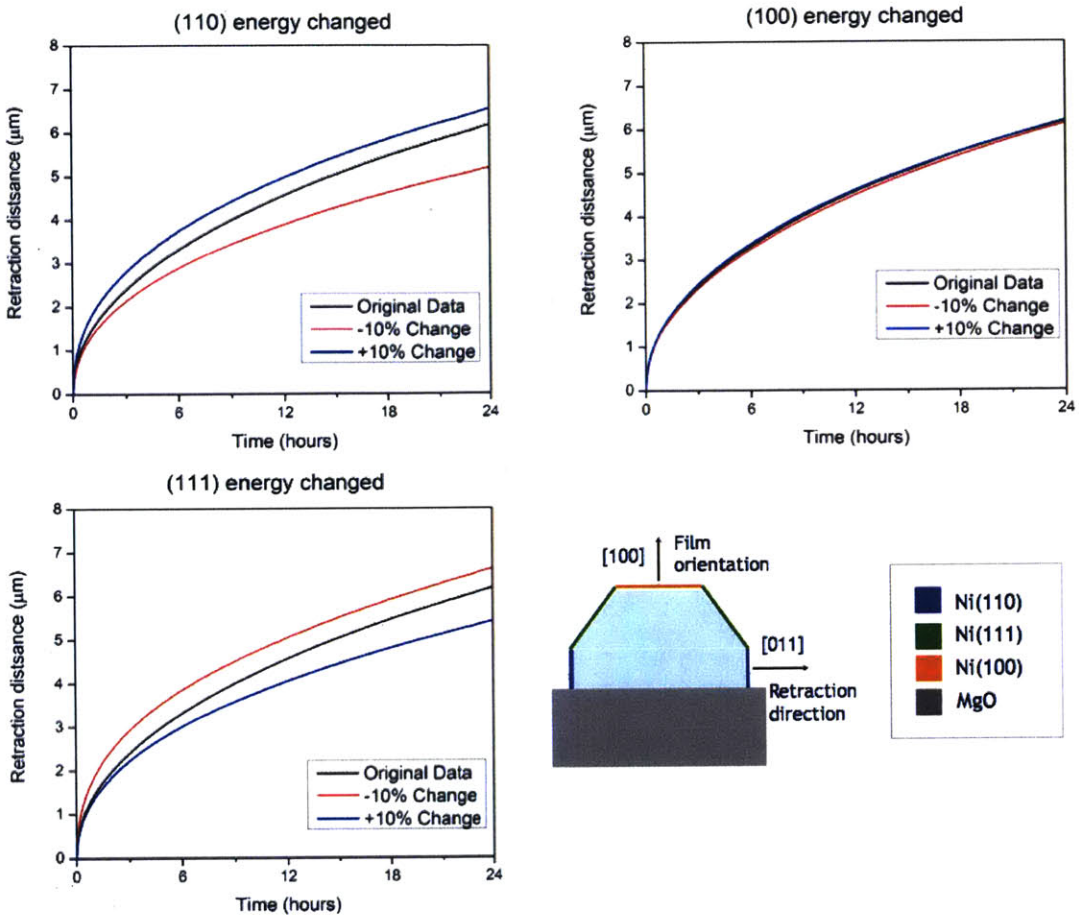

Figure 6-3. Sensitivity of edge retraction rate with respect to energy in Ni(100) films. For the given equilibrium shape, the retraction rate was measured after changing the facet energy as indicated in the figure.

Due to wider ranges of error in surface self-diffusivity data, adjusting the diffusivity led to a more significant change in the rate of edge retraction. Also, measurement of surface self-diffusivities are generally subject to a very large range of error and reported values also are often significantly different in different studies [36, 37, 44-46]. The diffusivities in the model were systematically adjusted within the error ranges to observe possible improvement in the fit. When the model overestimated the experimental data, the diffusivity with the largest magnitude was first adjusted for each case. When the maximum range of error was reached, the diffusivity with the second largest magnitude was adjusted, and the third diffusivity was adjusted after the maximum range of error for the previous diffusivity was reached. When the model underestimated the experimental data, the diffusivity with the smallest magnitude was first

adjusted. The agreement indeed improved significantly, as illustrated in Figure 6-4. In (a), the (111) diffusivity was decreased by 80%, the (110) diffusivity was decreased by 55%, and the (100) diffusivity was decreased by 70%. In (b), the (100) diffusivity was increased by 15% and the (110) diffusivity was increased by 80%. In (c), the (111) diffusivity was decreased by 60%. All adjustments were within the range of error provided in Table 5-1. It should be noted that the time scaling of retraction distance was not affected by changes in the diffusivity values.

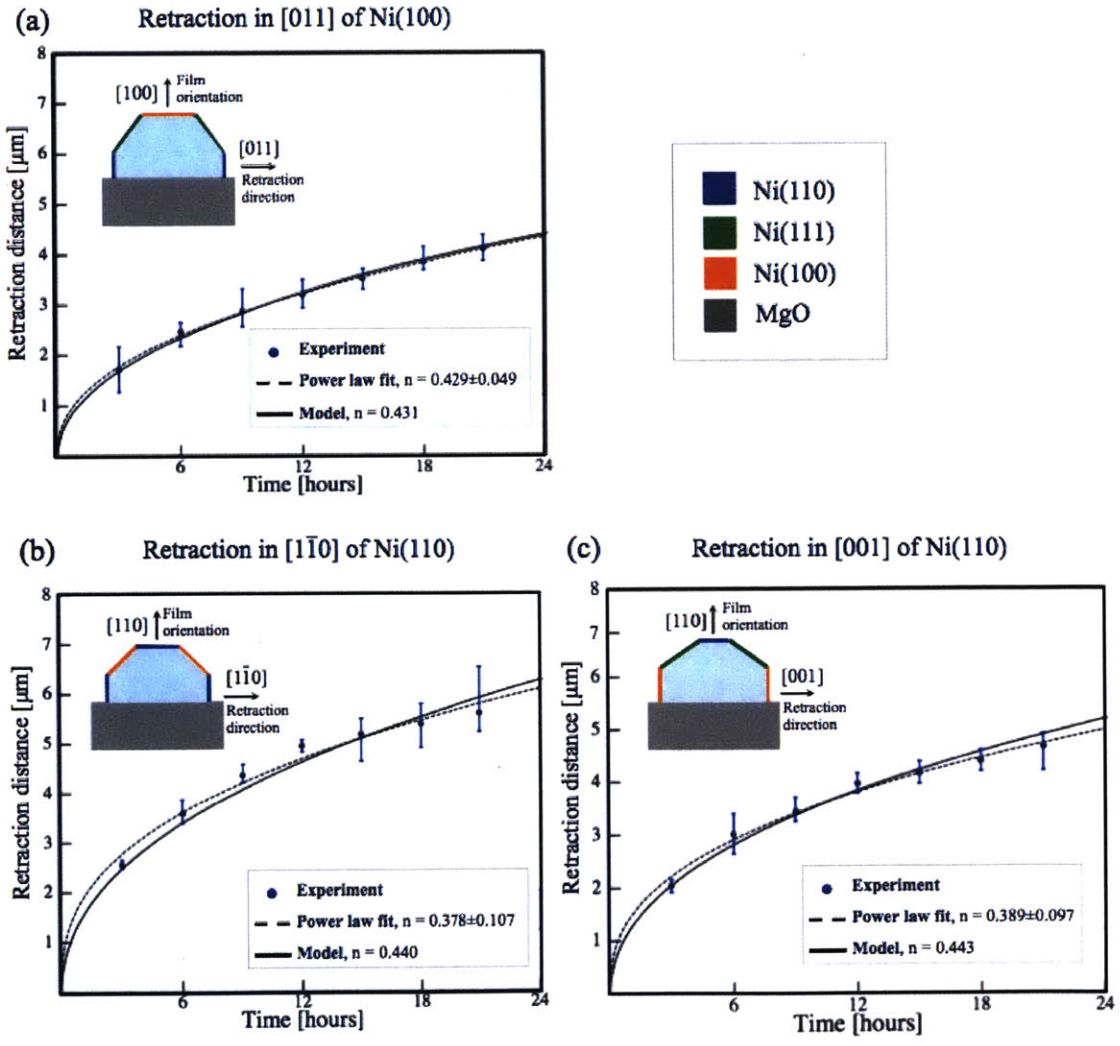

Figure 6-4. Experimental results and the model fitted through adjustment of diffusivities within the ranges of the experimental error of their determination. In (**a**), diffusivities on the (111), (110), and (100) facets were adjusted. In (**b**), the diffusivities on the (100) and (110) facets were adjusted. In (**c**), the diffusivity on the (111) facet was adjusted.

Using the measured experimental data, kinetic Wulff plots for retraction of kinetically stable edges, similar to those in Figure 1-8, in Ni(100) and Ni(110) films could be obtained for all orientations at different times, as shown in Figure 6-5. It should be noted that throughout retraction, the anisotropy in retraction distance and retraction rate is consistent.

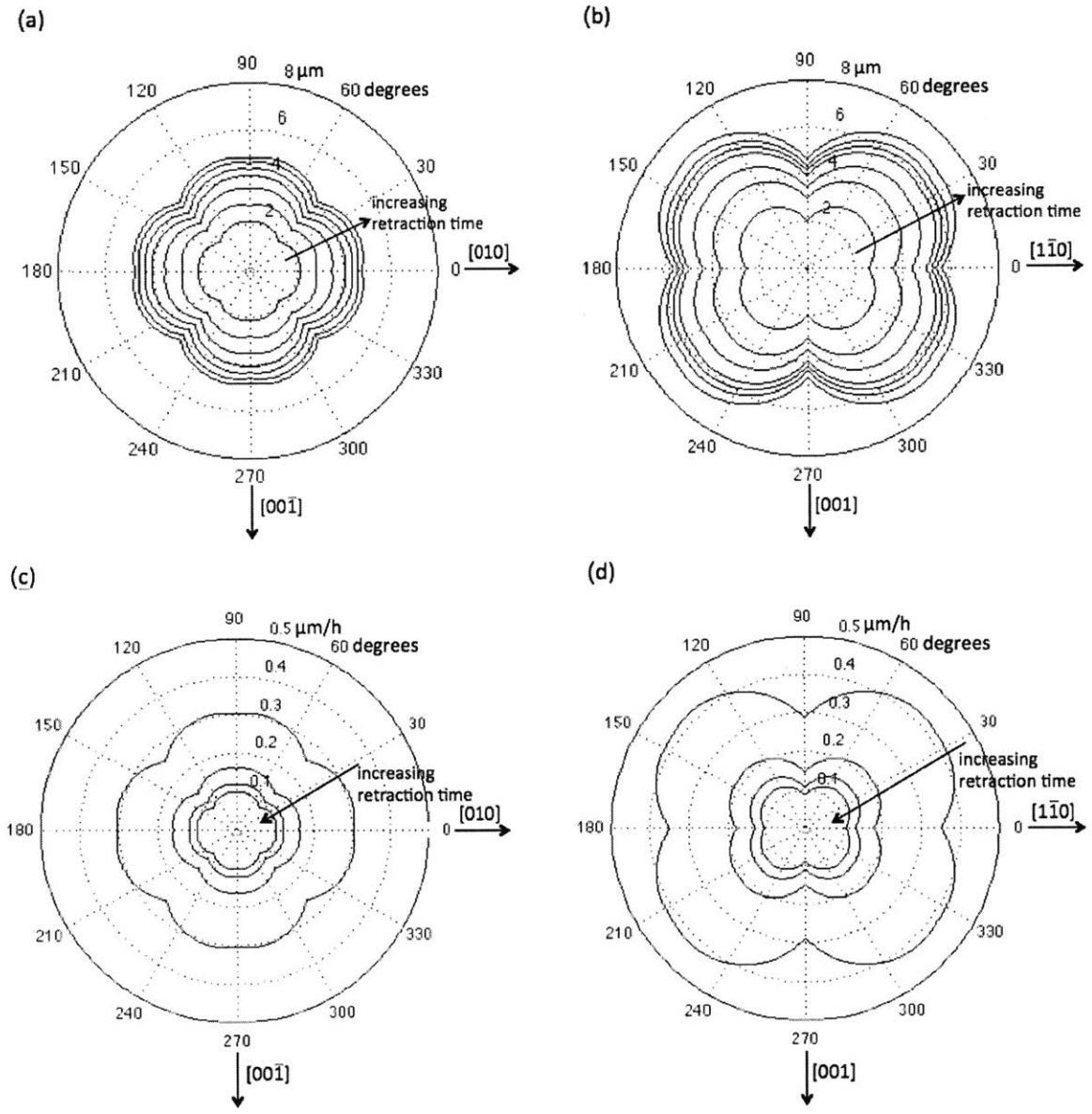

Figure 6-5. Kinetic Wulff plots constructed from the measured experimental data. (**a**) and (**b**) Edge retraction distances at specific times in (**a**) Ni(100) and (**b**) in Ni(110) films. Measured retraction times are 3, 6, 9, 12, 15, 18, and 21 hours, respectively. (**c**) and (**d**) Edge retraction velocity at specific times in (**c**) Ni(100) and (**d**) Ni(110) films. Measured retraction times are 3, 9, 15, and 21 hours, respectively.

Along with the possibility of error in the parameters used in the model, the assumption of completely faceted structures bound by equilibrium facets in the simulation may have led to the disagreement in the model and the experiment. Figure 4-5 shows SEM images of cross-sections of retracting rims after a 21-hour anneal. As can be seen in the figure, nonequilibrium facets also appear during retraction. Retracting rims are also not completely faceted. Higher index planes have more ledges and kinks, and thus have larger surface energy due to more dangling bonds and smaller diffusivity due to Schwoebel barriers [47]. Knowing that the maximum anisotropy difference between the lowest energy and the highest energy is approximately 3% [39], as shown in Figure 6-6, which is smaller than the range of error for the given surface energies, it can be said that the effect of the surface energy change is insignificant.

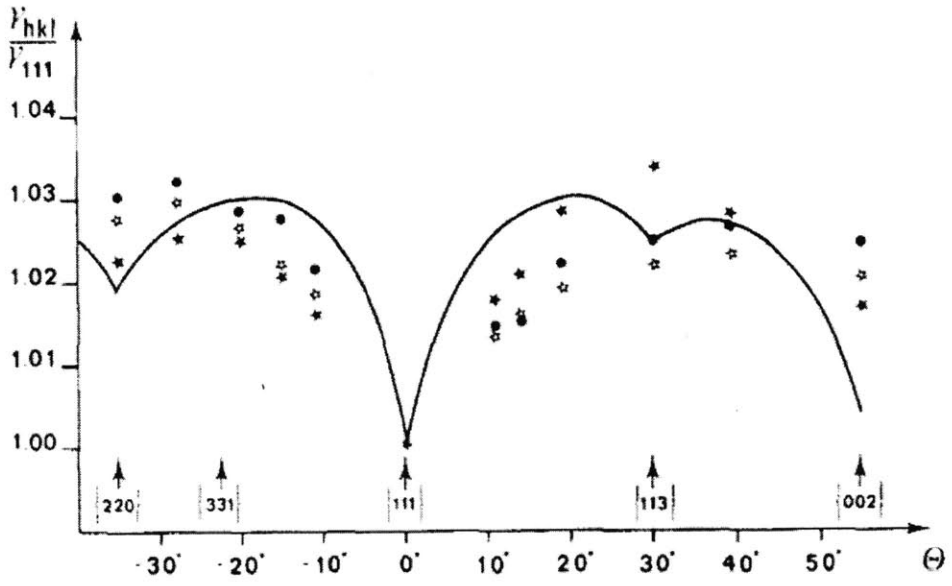

Figure 6-6. Surface energy anisotropy of Ni relative to surface energy of Ni(111) at 1200K, after Barsotti et al. [39]. Each set of points indicates different experimental measurements and the solid curve indicates the theoretical value of anisotropy obtained from the theoretical data by Drechsler and Nicholas [48]. It can be seen that the maximum anisotropy difference is about 3% of the Ni(111) energy.

Diffusivity, on the other hand, can lead to a significant difference in the result. From Figure 6-1, it can be found that in the cases in which the simulation overestimated the most (Figures 6-1(b) and (d)) the 2-dimensional equilibrium shapes have (111) facets, which have the highest diffusivity. In fact, unlike the assumptions in the simulation, a significant portion of the facets is replaced by higher index planes which have much lower diffusivities. This effect is less significant when the equilibrium shapes, instead of (111), have facets with more ledges and/or kinks, such as (100) or (110) (See Figures 4-5(a) and (c)). As can be seen in Figures 6-1(a) and (c), there is less overestimation by the simulation. Underestimation of retraction in the $[1\bar{1}0]$ direction in Ni(110) films may be understood in terms of the formation of deepening valleys behind the retracting rims, which are not taken into account in the simulation. Ni(110) films are known to form valleys behind retracting rims [20], and this may offer one explanation for underestimation ($[1\bar{1}0]$ retraction in Ni(110)) or less overestimation ([001] retraction in Ni(110)).

Aside from the fact that nonequilibrium facets also are present during edge retraction and this may lead to a disagreement between the simulation and the experiment, there are other possible sources of discrepancy. It has been experimentally shown that the equilibrium shape of Ni is sensitive to the level of oxygen concentration during annealing [34]. As illustrated in Figure 6-7, depending on the oxygen concentration and the level of impurity originating from the tube furnace, different equilibrium facets may appear. In this thesis, a conventional tube furnace with a high flow rate of reducing gas (5% H_2 and 95% N_2) was used and thus it was assumed that Figure 6-7(b) most closely represents the equilibrium Wulff shape in the experiment. However, exact direct measurement of the equilibrium shape is necessary to confirm the actual equilibrium shape as it is sensitive to the level of impurities.

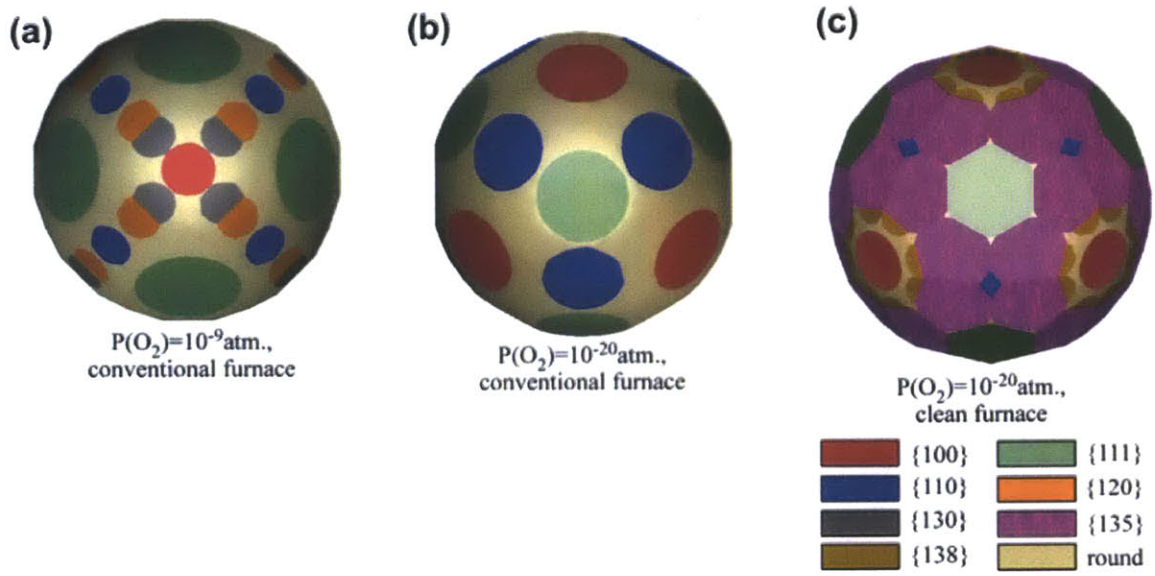

Figure 6-7. Equilibrium Wulff shape of Ni particles in different annealing conditions, as provided, after Meltzman et al. [34]. The facets appearing in the equilibrated particles are different when annealed in different oxygen concentration and impurity level.

Initially, the patterned edges are not composed of equilibrium facets. It is only after the rims have retracted for a while that facets appear on the rims. As shown by Ye and Thompson [21], faceting of retracting rims require a finite length of time that is long enough to affect the retraction of edges compared to the scope of annealing experiments. Also, as can be seen from the expression for the time for a particle to reach its equilibrium shape provided by Nichols and Mullins [49],

$$\tau = \frac{r^4 kT}{24\gamma_{fv} D \upsilon \Omega}, \tag{6-1}$$

where r is the particle radius, kT the thermal energy, and γ_{fv} the surface energy, D the diffusivity, υ the number of atoms per unit area and Ω the atomic volume, the time to equilibration is also dependent on the facet energies and diffusivities. Therefore, different edges may require different times to develop facets, which can also contribute to the discrepancy between the experiments and the model based on the method of crystalline formulation. Measurement of faceting time, however, may be tricky because a high enough time resolution is needed and thus a large number of annealing steps are required or an in-situ measurement has to be made.

6.2. Summary

In this chapter, the measured experimental data and the modeling results were compared. Some degree of discrepancy between the model and the experiment was observed, and possible sources of error were identified. It was found that during the retraction of edges, nonequilibrium facets also appear, and because such facets have higher surface energy and lower surface self-diffusivity, they can contribute to the divergence from the model, in which only equilibrium facets are present throughout the morphological evolution. Other possible sources of error include formation of local valleys behind retracting rims in Ni(110) films, which the simulation does not allow, changes in equilibrium shapes due to changes in oxygen concentration and impurity levels during annealing, and differences in the times required for facet formation for rims retracting in different directions, resulting from anisotropic surface energies and diffusivities.

Chapter 7. Conclusion

Quantitative analysis and understsanding of solid-state dewetting in thin single crystal films is critical if dewetting is to be used as a potential self-assembly method capable of producing regular patterns much smaller than the initial templates. In this thesis, a quantitative analysis of capillarity-driven anisotropic edge retraction of kinetically stable edges, which are defined as the edges in orientations that do not develop in-plane facets during retraction, during solid-state dewetting in 130-nm thick single crystal Ni(100) and Ni(110) films was conducted.

In Chapter 4, rates of edge retraction in kinetically stable orientations were measured and analyzed. Kinetically stable facets remain straight as they retract. Edges with other in-plane orientations break up into in-plane facets composed of segments with kinetically stable orientations. When the rates of edge retraction in kinetically stable orientations are known, the retraction rates in other orientations can be easily obtained using a simple geometric construction. While experimentally determined retraction rates were different for different crystallographic orientations with different bounding facets, the time scaling of the retraction rates was the same within experimental error. The retraction distance x_o was found to scale as $x_o \propto t^n$ with n~0.4. The measurements were consistent with previous studies conducted under the same experimental conditions and showed that the natural holes are bound by the slowest retracting edges before they are subject to further dewetting instabilities such as pinch-off, a fingering instability, or a corner instability, which further complicate the dewetting morphology at later stages.

In Chapter 5, a 2-dimensional model capable of dealing with edge retraction in kinetically stable orientations was developed using the crystalline formulation method developed by Carter et al. [24] and modified to introduce substrates in collaboration with Rachel V. Zucker in Professor Carter's Group at MIT. To apply this method, it was assumed that the shape of interest is completely faceted throughout the course of morphological evolution and that only equilibrium facets satisfying the local equilibrium condition appear during edge retraction. Although the 2-dimensional nature of the model limits its use to the cases where the retracting edges whose facet normals are in-plane with the retraction direction, it still provides a useful prediction and explanation of the edge retraction and captures the physics of rim formation during retraction. As

in an earlier study, the time scaling of the retraction distance was found to follow n~0.44. Also, it was found that this scaling is independent of the crystallographic orientation and facets of the edge, and also of the values taken for the surface energies and diffusivities. The scaling is also similar to what is found in simulations using isotropic surface energies (n~0.40).

In Chapter 6, comparisons of the measured experimental data and the modeling results were made. While the time scaling of the observed and simulated retraction rates was independent of the crystallographic orientation of the edge, the magnitudes of the retraction rates were dependent on the crystallographic orientation of the edge. This dependence could be captured by making minor adjustments of the surface self-diffusivities of different facets, within their ranges of error. Also, it was found that during the retraction of edges, nonequilibrium facets appear, and because such facets have higher surface energy and lower surface self-diffusivity, they can contribute to the overestimation by the model where only equilibrium facets are present throughout the morphological evolution. Also, in Ni(110) films valleys form ahead of the retracting rims while this is not allowed in the simulation. Other possible sources of error include changes in equilibrium shapes due to changes in oxygen concentration and other impurity levels during annealing, and different times required for facet formation on edges retracting in different directions, with different surface energies and diffusivities.

While the model in its current form cannot account for all of the observed phenomenology, it provides a useful guide for interpretation of experimental results. Although the study presented in this thesis will act as a good starting point for the quantitative analysis of solid-state dewetting in single crystal films, much study of other dewetting phenomenologies is still needed. Given sufficient quantitative understanding of the mechanisms of solid-state dewetting of thin single crystal films, templated solid state dewetting can be used as a self-assembly method and a new patterning technique to make complex structures at sub-lithographic length scales.

Chapter 8. Future Work

As mentioned in Chapter 6, some sources of error originate from discrepancy between the assumptions in the simulation and what actually happens in the experiment. Although it was assumed that the rim is bound by equilibrium facets throughout the morphological evolution, it was shown that nonequilibrium facets also appear during retraction. To increase the accuracy of the model by taking this into consideration, it should be confirmed that each facet is present throughout the course of retraction, and this can be done by an in-situ observation of edge retraction. The finite time to rim faceting, which may also contribute to the error, can also be accurately measured by in-situ measurements.

Once dewetting starts from edges by capillarity-driven edge retraction, more dewetting instabilities occur. One interesting dewetting instability is mass shedding or pinch-off phenomenon. In the edge retraction simulations for films with isotropic surface energies and diffusivities, it was observed [14, 16, 17] that in the later stage of edge retraction, valleys form behind the retracting edge. When the depth of the valleys becomes large enough to reach the film-substrate interface, the retracting edge is separated from the remainder of the film and the newly developed edge again begins to retract, leaving a long wire behind. A schematic diagram of the simulation results is illustrated in Figure 8-1.

As the edges of a patch (a patterned film with two retracting edges) retract, valleys are formed ahead of the two edges. If the valleys merge at an early stage, they can disappear and a single wire is formed. For wider patches, the valleys might merge to form a single valley that continues to deepen and pinch off to form two wires. If the patch is even wider and the individual valleys reach the interface before they merge, three wires are formed, as illustrated in Figure 8-1. If the inner patch left for further retraction after the retracting edges pinch off is wide enough to have another pinch-off, it is possible to form four wires, etc.

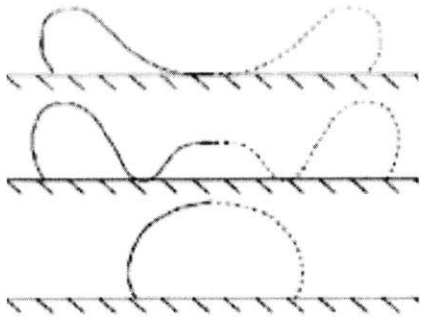

Figure 8-1. Formation of one, two or three wires by pinch-off, after Dornel et al [17].

Ye and Thompson [20] experimentally observed that as natural holes propagate in Ni(110) films, the deepening valleys behind the retracting edges pinch off to form more complex morphologies, as illustrated in Figure 8-2(a). As holes further propagate, the newly formed edges again pinch off, and this periodic mass shedding continues to form crystallographically oriented wires (Figures 8-2(b) and 8-2(c)).

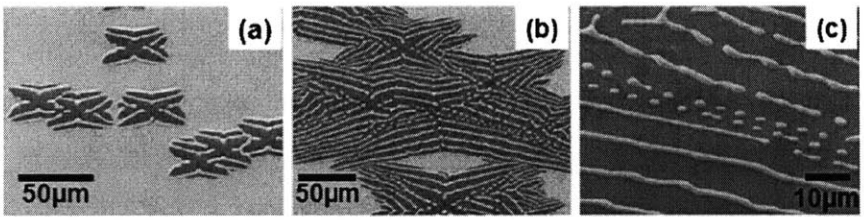

Figure 8-2. Pinch-off of growing holes in Ni(110) films, after Ye and Thompson [20].

No systematic quantitative study of this pinch-off behavior, however, has been conducted thus far, and this will also be an interesting dewetting phenomenology to be analyzed.

The inherent energetic instability of cylinders was first discussed by Plateau [50] and Lord Rayleigh [51]. A few years after Plateau experimentally observed the existence of the instability, Lord Rayleigh, analyzing the stability of a long cylindrical liquid jet subject to perturbations along the axis of the cylinder, proved mathematically that such a cylinder with an isotropic surface energy is inherently unstable and will develop a perturbation of wavelength larger than the circumference of the cylinder. This behavior and understanding was later shown to be

applicable to explain the phenomenon of field-emitter tip blunting and spheroidization by Nichols and Mullins [49], who showed in a kinetic analysis of a solid cylinder that the Rayleigh instability leads to the formation of beads from the cylinder.

An instability similar to the Rayleigh instability has also been shown to occur experimentally in solid-state dewetting of thin films, and is commonly referred to as a Rayleigh-like instability. In polycrystalline films, Jiran and Thompson [13] observed the formation of islands from fingers in the later stage of dewetting. Also, more experimental work has been conducted by Santala and Glaeser [52] in which the anisotropic Rayleigh instability of pore channels in different crystallographic orientations in sapphire was analyzed. Although the patterns on substrates are not likely to be completely cylindrical, the study shows that long wire patterns of thin films are also unstable under specific conditions.

Regarding single crystal films with anisotropic surface energies, there has been some effort to mathematically analyze the Rayleigh-like instability with anisotropic surface energies. Cahn [53] analyzed the stability of a cylindrical rod with transverse isotropy in surface free energy about the axis of the cylinder, which means that the surface energy anisotropy is solely determined by the local surface tilt against the axis of rod. The analysis by Cahn was further expanded by Stolken and Glaeser [54] where the effects of surface energy anisotropy on the kinetics of the development of the Rayleigh instability were examined. Gurski et al. [55] expanded this stability analysis to more general surface energy anisotropy. They further extended the numerical analysis of wire stability to wires with anisotropic surface energy now in contact with a substrate [56] and developed conditions for perturbations in different kinds of anisotropy with which the wires become unstable.

Although some simulations and numerical models have been developed to describe the Rayleigh-like instability in anisotropic materials, no known systematic experimental work has been done in the field of the Rayleigh-like instability of anisotropic thin-film materials. Quantitative characterization of the Rayleigh-like instability as a function of the crystallographic orientations of wires and comparison of experimental results with models will also be an interesting topic for study.

As previously mentioned, simulating the retraction of edges in orientations where no 2-dimensional equilibrium shapes are available requires development of a 3-dimensional model and thus is more complicated in the method of crystalline formulation. The abovementioned Rayleigh-like instability also requires a 3-dimensional model.

Kinetic Monte Carlo (KMC) simulations have satisfactorily predicted some dewetting phenomenologies in SOI structures [22, 23]. The basic concept of KMC is that the evolution of the system is considered as a movement of the whole system from one state to another, and during each transition the system takes a path with the shortest transition time, which is determined among the probabilistically determined transition times of all possible transition paths [57]. This significantly decreases the computational load and also extends the possible simulation time to the point where an appreciable degree of dewetting morphology is observable. One major drawback of this method is that it may not be able to correctly describe the phenomenology if the transition mechanism between the states is not well known [28, 57]. Because it is now generally accepted that surface self-diffusion is the dominant mechanism for solid-state dewetting, it is expected that under appropriate boundary conditions, KMC can be used to describe many dewetting phenomenologies with computational efficiency.

Reference

1. K. N. Tu, Annual Review of Materials Science **15**, 147-176 (1985).
2. C. Jahan, O. Faynot, L. Tosti and J. M. Hartmann, Journal of Crystal Growth **280**, 530-538 (2005).
3. J. Mizsei, Sensors and Actuators B **16**, 1-3 (1993).
4. M. Chhowalla, K. B. K. Teo, C. Duati, N. L. Rupesinghe, G. A. J. Amaratunga, A. C. Ferrari, D. Roy, J. Robertson and W. I. Mine, Journal of Applied Physics **90** (10), 5308-5317 (2001).
5. V. Schmidt, J. V. Wittemann, S. Senz and U. Gosele, Advanced Materials **21** (25-26), 2681-2702 (2009).
6. R. W. Balluffi, S. M. Allen and W. C. Carter, *Kinetics of Materials*. (Wiley and Sons, Hoboken, NJ, 2005).
7. C. Herring, Physical Review **82** (1), 87-93 (1951).
8. G. Wulff and Z. Krist, Physical Review **34** (449) (1901).
9. W. L. Winterbottom, Acta Metallurgica **15** (2), 303-310 (1967).
10. W. W. Mullins, Journal of Applied Physics **30**, 77-83 (1959).
11. D. J. Srolovitz and S. A. Safran, Journal of Applied Physics **60** (1), 247-254 (1986).
12. J. Ye, Massachusetts Institute of Technology, 2011.
13. E. Jiran and C. V. Thompson, Journal of Electronic Materials **19** (11), 1153-1160 (1990).
14. H. Wong, P. W. Voorhees, M. J. Miksis and S. H. Davis, Acta Materialia **48** (8), 1719-1728 (2000).
15. R. H. Brandon and F. J. Bradshaw, (R.A.E., Franborough, 1966).
16. D. J. Srolovitz and S. A. Safran, Journal of Applied Physics **60** (1), 255-260 (1986).
17. E. Dornel, J.-C. Barbe, F. d. Crecy, G. Lacolle and J. Eymery, Physical Review B **73** (11) (2006).
18. R. Nuryadi, Y. Ishikawa and M. Tabe, Applied Surface Science **159**, 121-126 (2000).
19. D. T. Danielson, D. K. Sparacin, J. Michel and L. C. Kimerling, Journal of Applied Physics **100** (8) (2006).
20. J. Ye and C. V. Thompson, Applied Physics Letters **97** (7) (2010).
21. J. Ye and C. V. Thompson, Acta Materialia **59** (2), 582-589 (2010).
22. E. Bussmann, F. Cheynis, F. Leroy, P. Muller and O. Pierre-Louis, New Journal of Physics **13** (2011).
23. F. Cheynis, E. Bussmann, F. Leroy, T. Passanante and P. Muller, Physical Review B **84** (245439) (2011).
24. W. C. Carter, A. R. Roosen, J. W. Cahn and J. E. Taylor, Acta Metallurgica Materialia **95** (12), 4309-4323 (1995).
25. L. Klinger, D. Amram and E. Rabkin, Scripta Materialia **64**, 962-965 (2011).
26. A. L. Giermann and C. V. Thompson, Applied Physics Letters **86** (121903) (2005).
27. D. Kim, A. L. Giermann and C. V. Thompson, Applied Physics Letters **95** (251903) (2009).
28. J. Ye and C. V. Thompson, Advanced Materials **23** (13), 1567-1571 (2011).
29. S. Chikazumi, Journal of Applied Physics **32** (3), S81-S82 (1961).
30. H. Qiu, A. Kosuge, H. Maruyama, M. Adamik, G. Safran, P. B. Barna and M. Hashimoto, Thin Solid Films **241** (1), 9-11 (1994).

31. P. Sandstrom, E. B. Svedberg, J. Birch and J.-E. Sundgren, Journal of Crystal Growth **197** (4), 209-217 (1999).
32. D. R. Gaskell, *Introduction to the Thermodynamics of Materials*, 5th ed. (Taylor and Francis Group, New York, NY, 2008).
33. R. Zucker, D. Chatain and W. C. Carter, Journal of Materials Science (2012).
34. H. Meltzman, D. Chatain, D. Avizemer, T. M. Besmann and W. D. Kaplan, Acta Materialia **59** (9), 3473-3483 (2011).
35. C. L. Cleveland and U. Landman, Journal of Chemical Physics **94** (11), 7376-7396 (1991).
36. P. S. Maiya and J. M. Blakely, Journal of Applied Physics **38** (2), 698-704 (1967).
37. J. M. Blakely and H. Mykura, Acta Metallurgica **9** (1), 23-31 (1961).
38. E. A. Clark, R. Yeske and H. K. Birnbaum, Metallurgical Transitions A **11** (11), 1903-1908 (1980).
39. T. Barsotti, J. M. Bermond and M. Drechsler, Surface Science **146** (2), 467-479 (1984).
40. G. Pacchioni and N. Rosch, Journal of Chemical Physics **104** (18), 7329-7337 (1996).
41. J. Chen and N. Chen, Journal of Physics: Condensed Matter **22** (21), 1-11 (2010).
42. J. E. Taylor, Acta Metallurgica Materialia **40** (7), 1475-1485 (1992).
43. R. V. Zucker, (Massachusetts Institute of Technology, Cambridge, 2012).
44. R. T. Tung and W. R. Graham, Surface Science **97**, 73-87 (1980).
45. E. E. Latta and H. P. Bonzel, Physical Review Letters **38** (15), 839-841 (1977).
46. J. R. Wolfe, University of Missouri-Rolla, 1968.
47. R. L. Schwoebel and E. J. Shipsey, Journal of Applied Physics **37**, 3682-3686 (1966).
48. M. Drechsler and J. F. Nicholas, Journal of Physics and Chemistry of Solids **28** (2609) (1967).
49. F. A. Nichols and W. W. Mullins, Journal of Applied Physics **36** (6), 1826-1835 (1964).
50. J. Plateau, *Experimental and Theoretical Statics of Liquids Subject to Molecular Forces Only*. (Gauthier-Villars, Paris, 1873).
51. L. Rayleigh, Proceedings of the London Mathematical Society **10** (4), 4-12 (1878).
52. M. K. Santala and A. M. Glaeser, Acta Materialia **56**, 1967-1980 (2008).
53. J. W. Cahn, Scripta Metallurgica **13**, 1069-1071 (1979).
54. J. S. Stolken and G. A.M., Scripta Metallurgica **27**, 449-454 (1992).
55. K. F. Gurski and G. B. McFadden, Proceedings of the Royal Society A **459**, 2575-2598 (2003).
56. K. F. Gurski, G. B. McFadden and M. J. Miksis, SIAM Journal on Applied Mathematics **66** (4), 1163-1187 (2006).
57. A. F. Voter, in *Radiation Effects in Solids*, edited by K. E. Sickafus, E. A. Kotomin and B. P. Uberuaga (Nato Publishing, Dordrecht, The Netherlands, 2005).